

THE ANGULAR MOMENTUM DISTRIBUTION OF GAS AND DARK MATTER IN GALACTIC HALOS

SANJIB SHARMA

Department of Physics University of Arizona, Tucson, AZ 85721, USA
 Astrophysikalisches Institut Potsdam, 14482 Potsdam, Germany

AND

MATTHIAS STEINMETZ¹

Astrophysikalisches Institut Potsdam, 14482 Potsdam, Germany
 Steward Observatory, University of Arizona, 933 N Cherry Ave, Tucson, AZ 85721, USA
Draft version May 23, 2019

ABSTRACT

We report results of a series of non radiative N-body/SPH simulations in a Λ CDM cosmology, designed to study the growth of angular momentum in galaxy systems. A sample of 41 halos of differing mass and environment were selected from a cosmological N-body simulation of size $32.5h^{-1}$ Mpc, and re-simulated at higher resolution with the tree-SPH code GADGET.

We find that the spin of the baryonic component correlates well with the spin of the dark matter, but there is a misalignment of typically 20° between these two components. The spin of the baryonic component is also on average larger than that of the dark matter component and we find this effect to be more pronounced at lower redshifts. A significant fraction f of gas has negative angular momentum and this fraction is found to increase with redshift. This trend can be explained as a result of increasing thermalization of the virializing gas with decreasing redshift. We describe a toy model in which the tangential velocities of particles are smeared by Gaussian random motions. This model is successful in explaining some of the global angular momentum properties, in particular the anti-correlation of f with the spin parameter λ , and the shape of the angular momentum distributions.

We investigate in detail the angular momentum distributions (AMDs) of the gas and the dark matter components of the halo. We compare and contrast various techniques to determine the AMDs. We show that broadening of velocity dispersions is unsuitable for making comparisons between gas and dark matter AMDs because the shape of the broadened AMDs is predominantly determined by the dispersion and is insensitive to the underlying non broadened AMD. In order to bring both gas and dark matter to the same footing, we smooth the angular momentum of the particles over a fixed number of neighbors. The AMDs obtained by this method have a smooth and extended truncation as compared to earlier methods. We find that an analytical function in which the differential distribution of specific angular momentum j is given by $P(j) = \frac{1}{j_d^\alpha \Gamma(\alpha)} (j)^{\alpha-1} e^{-j/j_d}$, where

$j_d = j_{tot}/\alpha$, can be used to describe a wide variety of profiles, with just one parameter α . The distribution of the shape parameter α for both gas and dark matter follows roughly a log-normal distribution. The mean and standard deviation of $\log(\alpha)$ for gas is -0.04 and 0.11 respectively. About 90–95% of halos have $\alpha < 1.3$, while exponential disks in NFW halos would require $1.3 < \alpha < 1.6$. This implies that a typical halo in simulations has an excess of low angular momentum material as compared to that of observed exponential disks, a result which is consistent with the findings of earlier works. α for gas is correlated with that for dark matter (DM) but they have a significant scatter $\langle \alpha_{Gas}/\alpha_{DM} \rangle = 1.09 \pm 0.2$. α_{Gas} is also biased towards slightly higher values compared to α_{DM} . The angular momentum in halos is also found to have a significant spatial asymmetry with the asymmetry being more pronounced for dark matter.

Subject headings: cosmology: dark matter—galaxies: formation—galaxies: structure

1. INTRODUCTION

Disk galaxies are rotationally supported systems and their structural properties are intimately linked to their angular momentum distribution. The standard picture of formation of disk galaxies is that the density perturbations grow due to gravitational instability and end up forming virialized systems of dark matter and gas. The gas cools and collapses towards the center (White & Rees 1978). The gas has angular momentum which it acquires due to tidal interactions. This can be quantified in terms of a dimensionless spin parameter $\lambda = J|E|^{1/2}/(GM^{5/2})$ (Peebles 1969) which has a value of about 0.05 (Efstathiou & Jones 1979; Barnes & Efstathiou

1987; Steinmetz & Bartelmann 1995). The angular momentum of the gas is conserved during the collapse resulting in the formation of a centrifugally supported disk, whose size is consistent with that of observed disk galaxies (Fall & Efstathiou 1980).

Based on the initial density profiles ($\rho = \rho(r)$) and angular momentum distributions ($m = m(j)$) or ($M_{<j} = M_{<j}(j)$) the final surface density of disks can be determined. Dalcanton, Spergel, & Summers (1997) derived the surface density of the disks assuming the halos to be uniform spheres in solid body rotation. From numerical simulations it is now known that density profiles of dark matter in halos follow a universal profile as described by Navarro, Frenk, & White (1996, 1997, NFW). Using these realistic profiles and assuming the final surface density of disks to be exponential Mo, Mao, & White (1998) investigated various properties of

Electronic address: ssharma@aip.de
 Electronic address: msteinmetz@aip.de

¹ David and Lucile Packard Fellow

disks like rotation curves, disk scale lengths and so on. They also addressed the issue of stability of disks. However, angular momentum distributions are required to more realistically model the surface density of disk galaxies. Bullock et al. (2001, henceforth B2001) have reported that in CDM simulations, the DM halos obey a universal angular momentum distribution of the form

$$\frac{M(< j)}{M_v} = \frac{\mu j}{j_0 + j} \quad (1)$$

where j is the specific angular momentum and $M(< j)$ is mass with specific angular momentum less than j . The shape parameter μ has a log-normal distribution and the 90% range is given by $1.05 < \mu < 2.0$. Assuming that the angular momentum profile of gas is identical to that of dark matter, B2001 calculated the surface density profiles of the resulting disks, and found that (for the range of μ given above) the resulting disks are too centrally concentrated compared to exponential profiles. In addition, detailed hydrodynamical simulations of gas collapse in hierarchical structure formation scenario exhibit the so-called “angular momentum catastrophe”: the gas component loses its angular momentum due to dynamical friction and ends up forming disks that are far too concentrated (Navarro & Benz 1991; Navarro & White 1994; Navarro & Steinmetz 1997; Steinmetz & Navarro 1999).

Recently van den Bosch et al. (2002) (henceforth vB2002) has tested the assumption, that the AMDs of gas and DM are similar, by directly measuring the AMDs of gas in proto galaxies from hydrodynamical simulations at $z = 3$. They find the spin parameter distribution of gas and dark matter to be identical in spite of the angular momentum vectors of gas and dark matter being misaligned by $\sim 35^\circ$. In order to compare the AMDs of gas and DM within halos, they broaden the velocities of gas to account for the microscopic random motions of gas atoms. The broadened profiles are found to be very similar to that of DM, though, as we are arguing later in this paper, this result is dominated by the dispersion hiding away the effect of the actual profiles.

vB2002 also demonstrated that a considerable amount of gas (between 5 and 50 percent) have negative angular momentum. Assuming that the gas with negative angular momentum combines with that of positive angular momentum to form a non rotating bulge, and the remaining positive angular momentum material ends up forming a disk, they found the surface density profiles of the resulting disks to closely follow an exponential profile. However the galaxies end up with a large B/D ratio, and with a minimum B/D of 0.1 the question of how to form bulge-less dwarf and LSB galaxies is still unanswered. The problem of an excess of low AM material gets transferred into a problem of excessive bulge formation.

To investigate these issues in more detail and to see if these properties have any evolution with redshift we perform a series of N-Body/SPH simulations of selected halos till $z=0$. Special care is taken to have high number of particles in the final virialized halos so as to measure the angular momentum accurately. The details of the simulation and methods of analysis are described in Sec-2. Results related to global angular momentum parameters and their evolution with redshift are presented in Sec-3. In Sec-4 we present a toy model to explain some of these findings. In Sec-5 and 6 we analyze the angular momentum distributions.

2. METHOD

2.1. Simulation

The cosmology adopted in the simulation is the so called concordance model of Λ CDM cosmology, in agreement with recent WMAP and SDSS results (Spergel et al. 2003; Melchiorri, Bode, Bahcall, & Silk 2003). The parameters adopted are $\Omega_\lambda = 0.7$, $\Omega_m = 0.3$ and $\Omega_b = 0.02235h^{-2}$ and a Hubble constant of $65 \text{ km s}^{-1} \text{ Mpc}^{-1}$. The power spectrum parameter determining the amplitude of mass fluctuations in a sphere of radius $8h^{-1} \text{ Mpc}$ was set to 0.9 and shape parameter Γ was set to 0.2. An AP^3M code was used to evolve 128^3 dark matter particles in a $32.5h^{-1} \text{ Mpc}$ cube from $z = 24$ to $z = 0$ using 2000 equal steps in expansion factor. At $z = 0$, 41 halos were selected with circular velocities ranging from 64 km s^{-1} to 310 km s^{-1} and masses ranging from $1.3 \times 10^{11} \text{ M}_\odot$ to $1.5 \times 10^{13} \text{ M}_\odot$. These halos were then re-simulated at higher resolution with more dark matter particles and also with an equal number of gas particles. The simulations were performed from $z = 50$ to $z = 0$. These re-simulations were done using the code GADGET (Springel, Yoshida, & White 2001). The gas particles were given an initial temperature of 100 K at $z = 50$ and an artificial temperature floor of 100 K was kept during the simulation. The number of particles (of each kind) within the virial radius ranges from $8000 - 80000$. A gravitational softening of $2 \text{ kpc } h^{-1}$ (physical) was used. The integration was performed in comoving co-ordinates.

2.2. Halo Identification

We adopt the method of vB2002 to identify the center of mass of a virialized region. We start with the densest gas particle as a guess for the center of mass and iteratively increase the radius till the average mass density enclosed by a spherical region is Δ_v times the mean matter density at that redshift. Δ_v is approximated by (Bryan & Norman 1998) $\Delta_v \simeq (18\pi^2 + 82x - 39x^2)/(1+x)$, where $x = \Omega_m(z) - 1$. We re-center the particles within the virial radius in velocities and position and then recalculate the virial radius based on this new center of mass. We repeat this process until the distance between the center of mass before and after the calculation of virial radius is less than 0.1 percent of the virial radius.

2.3. Angular momentum distributions

As discussed by vB2002, there are two kinds of velocities for particles in the simulations, the actual microscopic velocity \mathbf{v} of individual particles and the mean streaming velocity \mathbf{u} at any location \mathbf{x} . The actual microscopic velocity \mathbf{v} is given by equation $\mathbf{v} = \mathbf{u} + \mathbf{w}$, where \mathbf{w} is the particles random motion. For collisionless dark matter particles, which interact only through gravity, the velocity given by simulations is \mathbf{v} , whereas collisional gas (SPH) particles, the velocity given by simulations is \mathbf{u} , the information about the random motion is incorporated into the internal energy per unit mass U . If σ is one dimensional velocity dispersion of the particle, its temperature T is given by

$$U = \frac{3}{2}\sigma^2 = \frac{3}{2}\frac{kT}{\mu} \quad (2)$$

where μ is the mean molecular weight of gas. In order to compare the kinematical properties of the gaseous or dark matter component we either need to broaden the velocities of gas particles by using Eq. (2) (we label these by superscript t ; denoting the actual motion) or smoothen the velocities of dark matter particles by an appropriate smoothening length (we label these by superscript s ; denoting the streaming motion of the fluid).

The total angular momentum of gas or dark matter is given by

$$\mathbf{J}_{gas,DM} = \sum_{i=1}^{N_{gas,DM}} m_i \mathbf{r}_i \times \mathbf{v}_i \quad (3)$$

where \mathbf{r}_i and \mathbf{v}_i are the radius and velocity vectors respectively of a particle i , in a co-ordinate system in which both the position and the velocity of the center of mass of the entire halo (DM + gas) is zero. For the spin parameter, we use the modified definition of B2001.

$$\lambda_{gas,DM} = \frac{|\mathbf{j}_{gas,DM}|}{\sqrt{2}R_{vir}V_{vir}} \quad (4)$$

where j_{gas} and j_{DM} are the mean specific angular momentum of gas and dark matter respectively, and $V_{vir} = \sqrt{G(M_{gas}+M_{DM})/R_{vir}}$ is the circular velocity at virial radius R_{vir} . The misalignment θ between the angular momentum vectors of gas and dark matter \mathbf{J}_{gas} and \mathbf{J}_{DM} is given by

$$\cos\theta = \frac{\mathbf{J}_{gas} \cdot \mathbf{J}_{DM}}{|\mathbf{J}_{gas}| |\mathbf{J}_{DM}|} \quad (5)$$

We make a co-ordinate transformation such that the z-axis is aligned with the total angular momentum vector. For gas particles the z-axis is aligned along \mathbf{J}_{gas} while for dark matter z-axis is aligned along \mathbf{J}_{DM} . The z component of specific angular momentum j_z is then measured (henceforth we drop the subscript and denote it by j). The fraction of mass with $j < 0$ is labeled as f_{gas} and f_{DM} for gas and dark matter respectively. The differential angular momentum distribution (AMD) is the fraction of mass $P(j)$ with specific angular momentum between j to $j + dj$ i.e. $\int_{-\infty}^{\infty} P(j) dj = 1$. We define a parameter l which is related to j by

$$l = \frac{j}{\sqrt{2}V_{vir}R_{vir}} \quad (6)$$

(similar to definition in vB2002 except for a factor of $\sqrt{2}$). The above definition for l implies that

$$\int_{-1}^1 l P(l) dl = \lambda \quad (7)$$

The total specific angular momentum of a halo is denoted by j_{tot} and this is related to λ by $j_{tot} = \lambda \sqrt{2}R_{vir}V_{vir}$, see Eq. (4). The shape and extent of profiles depend on j_{tot} . With $s = j/j_{tot}$, as proposed in van den Bosch, Burkert, & Swaters (2001, henceforth BBS01), we obtain

$$\int_{-\infty}^{\infty} s P(s) ds = 1 \quad (8)$$

In most of our analysis we neglect the negative tail and define the distributions for the positive tail only and normalize with respect to it. The range of s or j in that case is from 0 to ∞ and for halos with negative tails the quantities like j_{tot} also need to be recalculated for the positive tail only. The cumulative angular momentum distribution $P(< j)$ is the fraction of mass with AM less than equal to j . It is also defined only for the positive tail, and is normalized with respect to it.

3. RESULTS

3.1. Global angular momentum parameters at $z=3$

As a first test we compare the results of our simulations against the analysis of vB2002, who compared various global

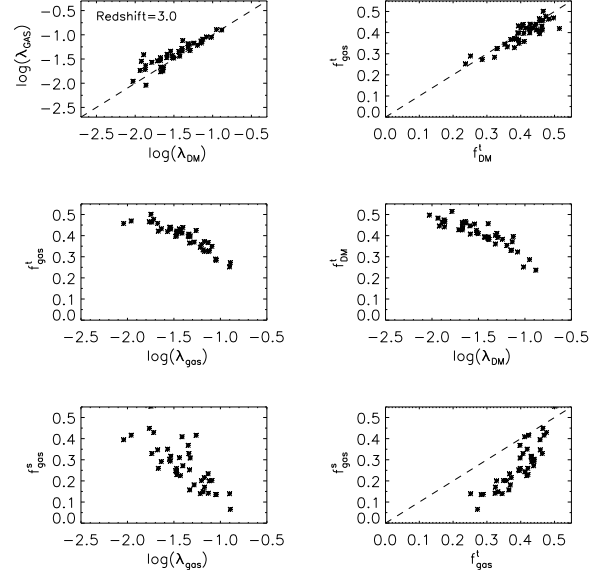


FIG. 1.— A comparison of various global angular momentum parameters at $z=3$ for both gas and dark matter. The parameters compared are the spin parameter λ and the fraction with negative angular momentum f . A comparison with Fig-2 of vB2002 shows that at $z=3$ the results of our simulations are in good agreement with the analysis of vB2002.

angular momentum parameters using a sample of 378 halos at a redshift of $z=3$ (see Fig-2 in vB2002). Our results for a sample of 41 halos at the same redshift, are shown in Fig. 1. We find them to be in good agreement.

The first plot on upper left compares λ_{gas} against λ_{DM} . λ of gas and DM are well correlated with a Spearman rank coefficient of $r_s = 0.88$, but show significant scatter. The mean of $\lambda_{gas}/\lambda_{DM}$ is 1.27 with a standard deviation of 0.40. This suggests that statistically the angular momentum acquired by gas and dark matter is similar but on a one-by-one comparison the spin parameters can be quite different. The fraction of matter with negative angular momentum for gas and dark matter denoted by f_{gas}^t and f_{DM}^t , are also well correlated with Spearman rank coefficient of 0.81 and $\langle f_{DM}^t/f_{gas}^t \rangle = 0.96 \pm 0.07$ (As described in Sec-2.3 the superscript t denotes inclusion of microscopic random motions while superscript s stands for streaming motions only). In the middle panels the strong anti-correlation of f_{gas}^t and f_{DM}^t with their respective spin parameters can be seen. In the lower left panel f_{gas}^s is also found to be anti-correlated with λ_{gas} . If we assume that the random motions are responsible for the negative angular momentum and that the ordered motion contributes to the λ , then this result is easy to understand. The more the ordered motion the less will be the effect of random motions. The plot of f_{gas}^s vs λ_{gas} is found to have more scatter than that of f_{gas}^t vs λ_{gas} which has broadened velocities. We will follow up on this though in more detail in section 4.

In the lower left plot f_{gas}^s is shown against f_{gas}^t . f_{gas}^s is less than f_{gas}^t as expected (because f_{gas}^t has more random motion) and the difference $f_{gas}^s - f_{gas}^t$ is found to increase at lower f values or at lower λ , respectively. A comparison of some of our results with vB2002 is given in Table 1.

3.2. Redshift dependence of angular momentum parameters

TABLE 1. GLOBAL ANGULAR MOMENTUM PARAMETERS

	vB2002	This paper
$\bar{\lambda}_{gas}$	0.039	0.040
$\bar{\lambda}_{DM}$	0.040	0.030
σ_{gas}	0.57	0.62
σ_{DM}	0.56	0.81
$\langle \lambda_{gas} - \lambda_{DM} \rangle$	-0.001 ± 0.020	0.006 ± 0.009
$\langle f'_g/f'_D \rangle$	0.97 ± 0.10	0.96 ± 0.07
$\langle \theta \rangle$	36.2	18.9

NOTE. — The properties shown above are for halos at $z = 3$, alongside are results from vB2002 also at same redshift. The results reported in this paper are in good agreement with vB2002

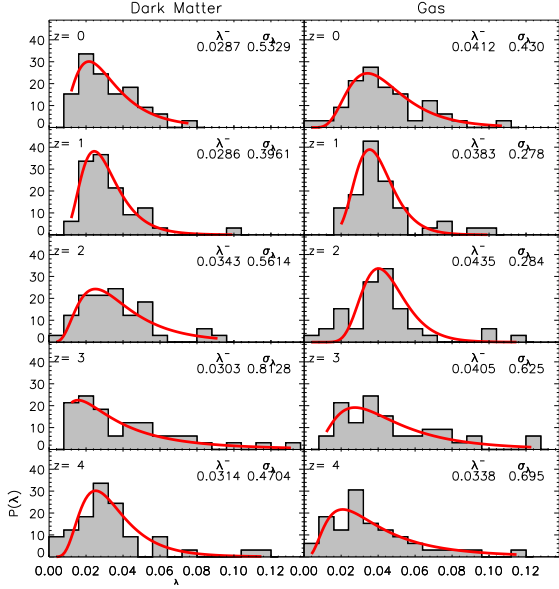


FIG. 2.— Distribution of spin parameter λ for dark matter (left) and gas (right) for a sample of 41 halos for redshifts ranging from 4 to 0. The solid line is the best fit log-normal distribution as given by Eq. (9). The fit parameters $\bar{\lambda}$ and σ_{λ} are also labeled on each of the plots.

Distribution of λ_{DM} and λ_{gas}

It has been suggested by numerous studies that the distribution of λ can be described by a log-normal distribution

$$p(\lambda)d\lambda = \frac{1}{\sqrt{2\pi}\sigma_{\lambda}} \exp\left(-\frac{\ln^2(\lambda/\bar{\lambda})}{2\sigma_{\lambda}^2}\right) \frac{d\lambda}{\bar{\lambda}}. \quad (9)$$

van den Bosch et al. (2002) have found that the gas and dark matter have very similar distribution of spin parameters. They found $\bar{\lambda}_{gas} = 0.039$ and $\bar{\lambda}_{DM} = 0.040$.

In Fig. 2 we have plotted the distribution of λ_{gas} and λ_{DM} for redshifts from 0 to 4. It is observed that $\bar{\lambda}_{DM}$ fluctuates between 0.029 to 0.034 while $\bar{\lambda}_{gas}$ seems to increase from 0.034 to 0.041 with decrease in redshift. The fact that λ_{gas} is higher than λ_{DM} can be seen more clearly in Fig. 3 where λ_{gas} is plotted against λ_{DM} . $\langle \lambda_{gas}/\lambda_{DM} \rangle$ is greater than 1 and increases as z decreases.

Distribution of Misalignment Angle θ

In Fig. 4 we show the misalignment angle between the total angular momentum vectors of dark matter and gas for various redshifts. The mean and median values are also shown in each

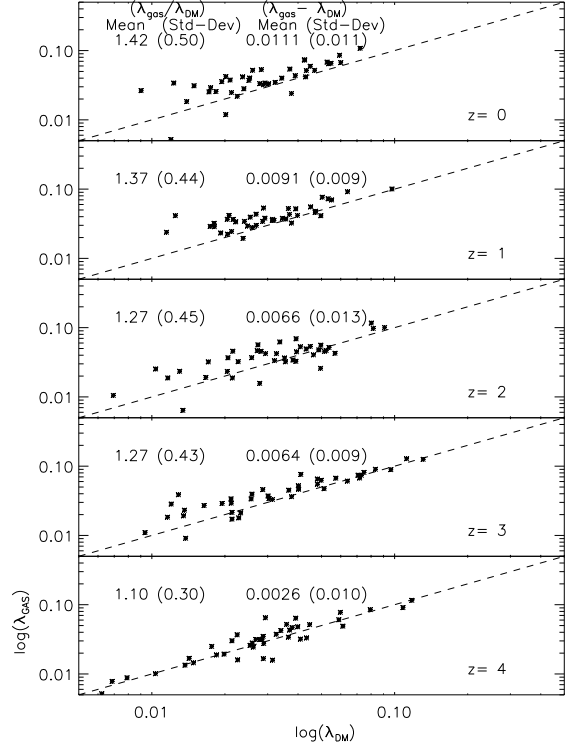


FIG. 3.— λ_{Gas} vs λ_{DM} for various redshifts. $\langle \lambda_{gas}/\lambda_{DM} \rangle$ and $\langle \lambda_{gas} - \lambda_{DM} \rangle$ along with their standard deviations are shown on each plot.

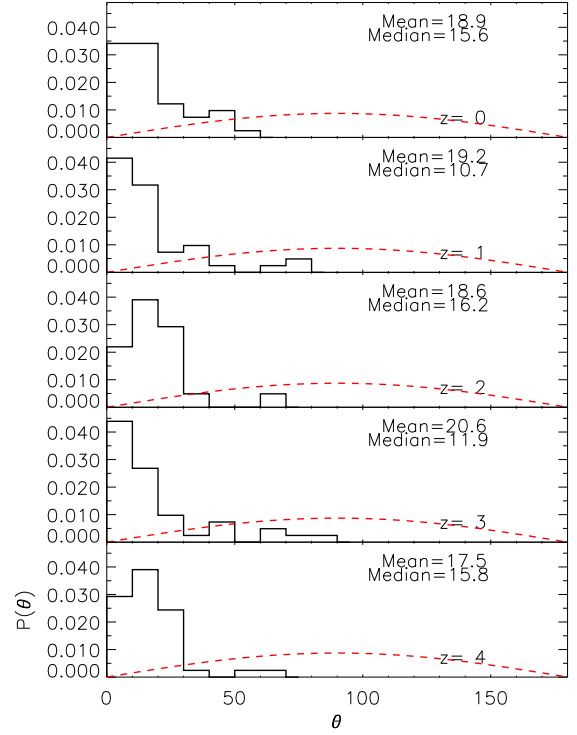


FIG. 4.— Distribution of misalignment angle θ for various redshifts. The dashed line is the expected distribution if the angle is completely random or uncorrelated.

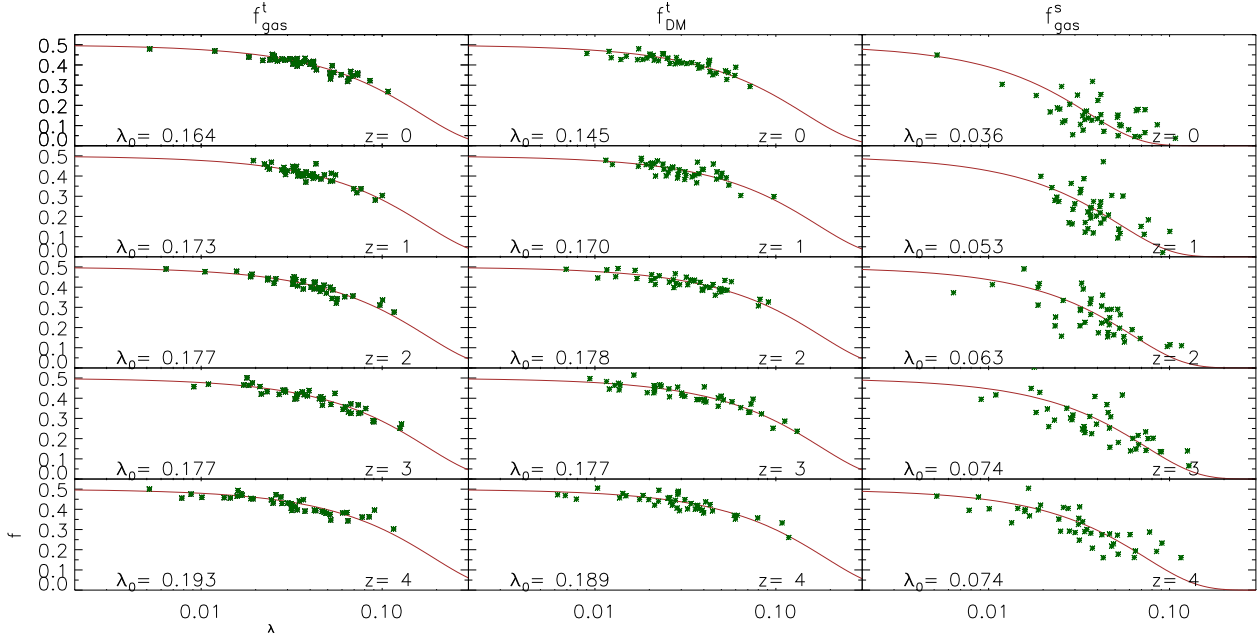


FIG. 5.— Counter-rotating fraction f as a function of spin parameter λ for various redshifts. Superscript t stands for analysis done with velocities which incorporate random motions and s stands for analysis done with streaming velocities. The solid lines are the fits given by the functional form in Eq. (10). The best value of parameter λ_0 is indicated on each plot.

panel. The distribution does not show any significant change with redshift. The mean value $\langle \theta \rangle$ is around 20 degrees.

Correlation of f with λ

As mentioned in Fig. 1, the fraction of matter with negative angular momentum f is anti-correlated with λ . We found that the f vs λ distribution can be well fit by a function of the form

$$f = 1 - I_g\left(\frac{\lambda}{\lambda_0}\right) \sim 0.5e^{-\lambda/\lambda_0} \quad (10)$$

where $I_g(x) = \int_{-\infty}^x \frac{e^{-t^2/(2\sigma^2)}}{\sqrt{2\pi}\sigma} dt$ is a Gaussian integral. The results of the applied fit are shown on each plot in Fig. 5. The anti-correlation can be described by a single parameter λ_0 . For the actual motion of both gas and DM, it is found that λ_0 is around 0.17 and does not seem to change much except for a decrease in its value at $z=0$. For streaming motion of gas the parameter λ_0 decreases consistently with decrease in redshift, thus hinting to a systematical change in the distribution of f_{gas} with redshift. Furthermore, the scatter in f vs λ plots corresponding to streaming motion of gas (column 3 Fig. 5) is quite large specially at lower redshifts as compared to the plots for broadened motions (column 1 and 2 Fig. 5).

3.3. Variation of $\langle f_{\text{gas}} \rangle$ with thermalization of gas

In Fig. 6 the distribution of f is plotted for various redshifts. It can be seen that the distribution for dark matter does not seem to change with redshift, while for gas it shifts towards smaller fractions of negative angular momentum material at lower redshifts. For DM $\langle f \rangle \sim 0.40$ while for gas $\langle f \rangle$ decreases from 0.33 to 0.15 monotonically with decrease in redshift (Fig. 7). The kinetic energy of gas particles in SPH simulation, is a combination of translational energy and internal (thermal) energy. The ratio $F_{Tr} = KE_{Tr}/(KE_{Tr} + KE_{Th})$ gives an estimate of thermalization. The lower the F_{Tr} the

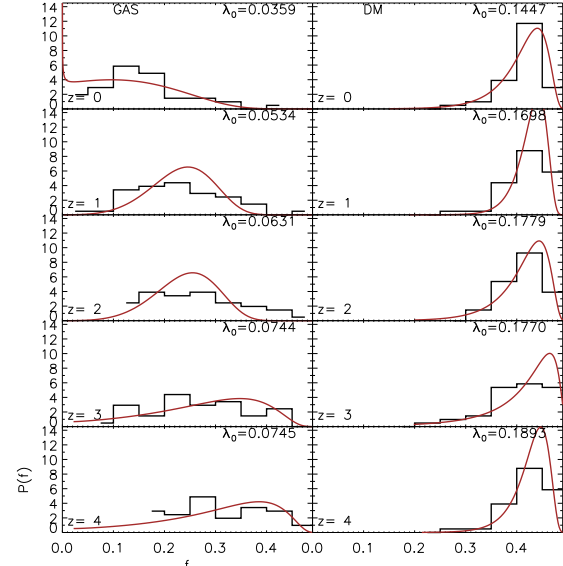


FIG. 6.— Distribution of counter-rotating fraction f for gas and dark matter for a sample of 41 halos. The distribution is almost independent of redshift for dark matter while for gas f is lower at lower redshifts. The solid line is the distribution as predicted by Eq. (25).

greater the thermalization. Fig. 7 shows that $\langle F_{Tr} \rangle$ just like $\langle f_{\text{gas}} \rangle$, also decreases monotonically with decrease of redshift. The correlation of $\langle F_{Tr} \rangle$ with $\langle f_{\text{gas}} \rangle$ is easy to understand.

The dispersion in velocity of particles gives rise to particles with negative angular momentum. For very small velocity dispersion of particles the fraction with negative angular momentum $f \sim 0$. If velocity dispersion is very large or AM is

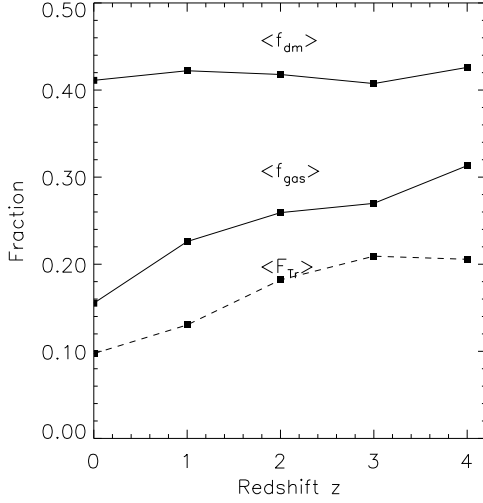


FIG. 7.— Counter-rotating fractions $\langle f_{\text{gas}} \rangle$, $\langle f_{\text{dm}} \rangle$ and the fraction of energy for gas in the form of translational motion $\langle F_{\text{Tr}} \rangle$, as a function of redshift. The average is taken over a sample of 41 halos. At lower redshifts the gas gets more and more thermalized, its kinetic energy getting converted into thermal, and this decreases $\langle f \rangle$.

very small, then $f \sim 0.5$. The SPH particles only have macroscopic flow velocities, the thermal energy is incorporated into U . For DM particles all the energy is in the form of velocities of particles. So f_{gas} is always less than f_{dm} . At higher redshift there are more mergers and the gas is more turbulent. As the redshift decreases, the gas undergoes relaxation and kinetic energy of gas gets converted into thermal energy. The velocity dispersion of gas decreases resulting in a decrement of f_{gas} . For dark matter $F_{\text{Tr}} = 1$ and $\langle f \rangle$ does not show any considerable evolution.

3.4. Effect of numerical resolution

To check whether the numerical resolution has an effect on f_{gas} we plot f_{gas} versus N , the number of gas particles in the halo (filled squares in Fig. 8) and find no correlation. To check the effect of numerical resolution in more detail 30 halos were re-simulated at a lower resolution with 1/8 times the original number of particles (open triangles in Fig. 8). The values of f do not show any systematic trend with change of resolution. Halos simulated in lower resolution have distributions of λ , f and misalignment angle θ (Fig. 9) identical to the distributions found in high resolution simulations. So the results shown above are robust to the effect of numerical resolution.

3.5. Evolution of gas particles having negative angular momentum

We investigate whether the gas that ends up with negative angular momentum also had negative angular momentum in the past. We identify a region in past that ends up in the virialized halo at $z=0$ by simply tracking halo particles at $z=0$ back in time. We re-center them, and then calculate their angular momentum. The fraction of particles with negative AM at any given stage during the evolution of this Lagrangian volume is a function of redshift so we denote it by $f_{\text{global}}(a)$. We identify a subset of particles that were counter rotating at $z=0$, and denote them by subscript $z=0$. The fraction of particles out of this subset that are counter rotating at any given instant is denoted by $f_{z=0}(a)$. Similarly $f_{z=15}(a)$ is the fraction

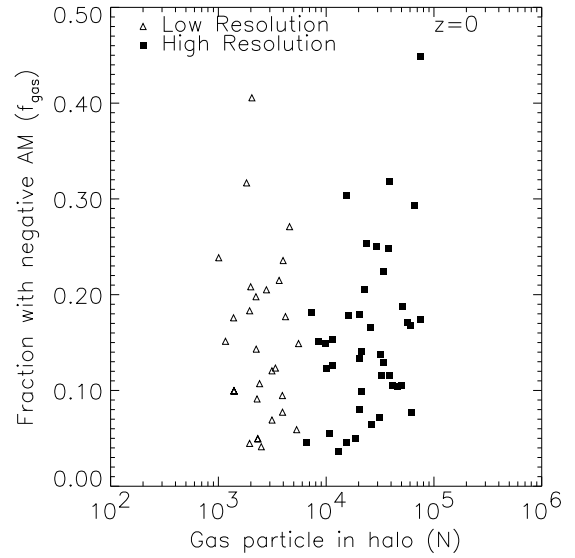


FIG. 8.— f_{gas} vs N_{gas} for halos at redshift of $z=0$ simulated at two different resolutions. The fraction f_{gas} does not show any apparent correlation with number of gas particles in the virialized halo indicating that this result is not affected by numerical resolution. The same set of halos re-simulated at 1/8 times the original resolution also do not show any systematic shift.

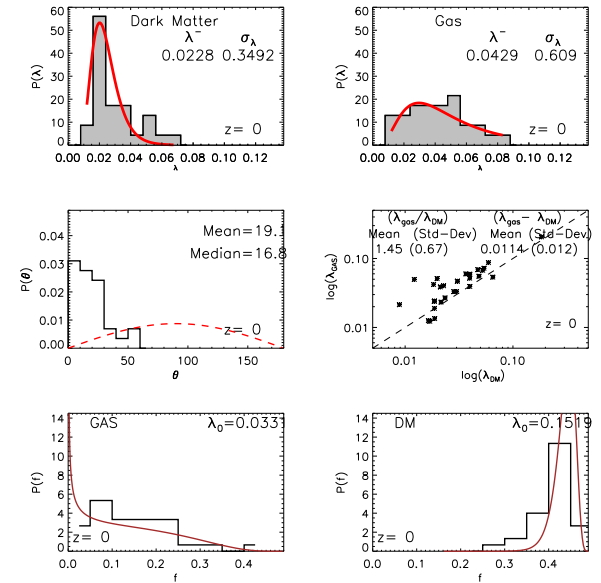


FIG. 9.— Various properties of halos and their distributions at $z=0$ from low resolution simulations (1/8 times the normal resolution). A comparison with Fig. 2, Fig. 3, Fig. 4, Fig. 6 which are the corresponding plots with high resolution simulations shows no difference.

of counter rotating particles out of a subset of particles that were counter rotating at $z=15$. If the particles with negative angular momentum at $z=0$ were also counter rotating at an earlier epoch, then they would have $f_{z=0}(a) \sim 1$ independent of redshift. Similarly if counter rotating particles at $z=15$ also had negative angular momentum later during their evolution then $f_{z=15}(a) \sim 1$. On the other hand if $f_{z=15}$ or $f_{z=0} \sim f_{\text{global}}$ then the particles are just a random subset drawn from the original halo and have no relation with their past or future, respectively.

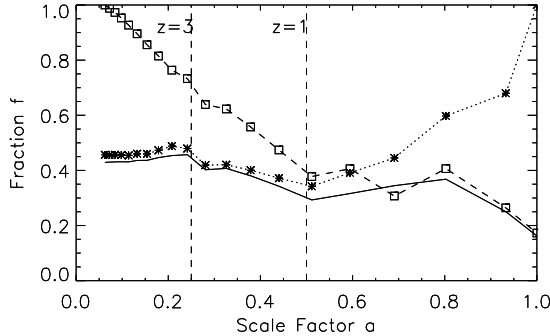


FIG. 10.— The evolution of fraction f of particles with negative angular momentum with scale factor a for various sub-components of gas. Solid line - f_{global} vs a , Dotted line (with stars) - $f_{z=0}$ vs a and Dashed line (with squares) - $f_{z=15}$ vs a . f_{global} is the fraction of gas with negative angular momentum for the whole halo. $f_{z=0}$ is the corresponding fraction out of a subset of particles that had negative angular momentum at $z = 0$. $f_{z=15}$ is the fraction out of a subset of particles that had negative angular momentum at $z = 15$.

In Fig. 10 we have plotted f_{global} , $f_{z=0}$ and $f_{z=15}$ as a function of scale factor a of the universe for a randomly selected halo. $f_{z=0}$ and $f_{z=15}$ are both close to 1 at their respective ends but by $z = 1$ both fractions have dropped to f_{global} and continue to remain so in respective directions. This suggests that particles that are counter rotating at a given instant will not necessarily counter rotate at a later epoch in future but will instead get mixed up randomly with the remaining portion of the halo.

4. A TOY MODEL: GAUSSIAN SMEARING OF ORDERED VELOCITIES (GSOV)

To get a better intuitive understanding of some of the results presented so far, in particular the anti-correlation of f with λ , we present here a toy model that describes the motion of the particles in the halo. We take a co-ordinate system with the z axis pointing along the direction of the total angular momentum vector. The actual velocity \mathbf{u} of a particle consists of the ordered motion $v_o \hat{\phi}$ (which is motion in circular orbits at a constant speed v_o), superimposed by random motions \mathbf{v}_σ . Each component of random motion \mathbf{v}_σ is drawn out from a Gaussian distribution with a dispersion σ . The random motions are assumed to be isotropic. \mathbf{u} can be written as

$$\begin{aligned} \mathbf{u} &= v_o \hat{\phi} + v_{\sigma_x} \mathbf{i} + v_{\sigma_y} \mathbf{j} + v_{\sigma_z} \mathbf{k} \\ &= (v_o + v_{\sigma_\phi}) \hat{\phi} + v_{\sigma_\rho} \hat{\rho} + v_{\sigma_z} \mathbf{k} \end{aligned} \quad (11)$$

According to this model the histogram of u_ϕ in a halo is given by

$$P(u_\phi) du_\phi = \frac{1}{\sqrt{2\pi}\sigma_\phi} e^{-(u_\phi - v_o)^2/(2\sigma_\phi^2)} du_\phi \quad (12)$$

In Fig. 11 we have plotted the histogram of u_ϕ for various halos, for both dark matter and gas. For most halos the u_ϕ distribution of gas particles can be well described by a Gaussian. Some halos are biased either to right or left, and some show two peaks which can be described by two Gaussian functions. A closer examination reveals that these peculiarities are associated with substructure of halos. For dark matter σ is large and this washes out any peculiarities that may have been present, consequently no significant deviation from the single Gaussian structure can be observed. Sometimes a slightly sharper peak compared to a Gaussian distribution can be seen indicative of a velocity dispersion that is not strictly isothermal.

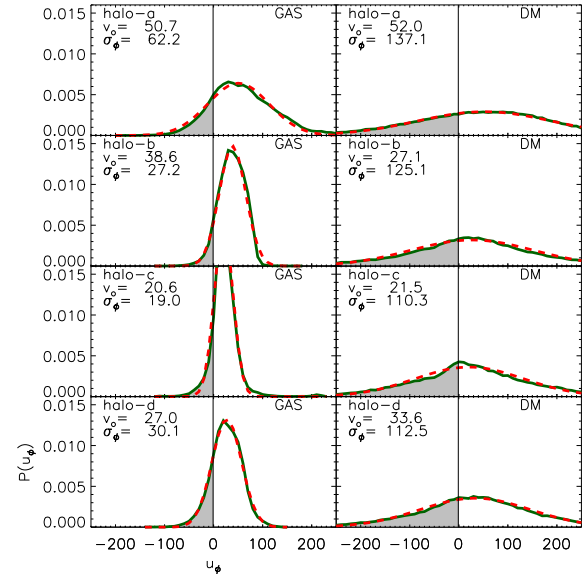


FIG. 11.— A plot showing distribution of u_ϕ for gas and DM for four different halos. Solid line: the histogram for particles in simulation, Dashed line: A Gaussian fit to the above histogram . The shaded region corresponds to particles with negative angular momentum.

In terms of this model the motion within a halo can be described by two parameters v_o and ζ where $\zeta = \frac{\sigma_\phi}{v_o}$. ζ is a measure of random motion relative to ordered motion. We calculate v_o and σ_ϕ for simulated halos by fitting a Gaussian profile as given by Eq. (12) to the histogram of u_ϕ . Fig. 12 shows the distribution of ζ and v_o/V_v for both gas and DM at $z = 0$. $\log(\zeta)$ can be fit by a Gaussian both for DM and gas. For gas $\zeta \sim 1$ while for DM $\zeta \sim 5$.

If the above model of Gaussian smearing is a realistic representation then the fraction of matter with negative angular momentum is simply the probability that u_ϕ is less than zero, i.e. v_{σ_ϕ} is less than $-v_o$ (Fig. 13). This can be expressed by an integral

$$\begin{aligned} f(v_o, \sigma_\phi) &= \int_{-\infty}^{-v_o} \frac{e^{-v^2/(2\sigma_\phi^2)}}{\sqrt{2\pi}\sigma_\phi} dv \\ &= 0.5[1 - \text{Erf}(\frac{1}{\sqrt{2}} \frac{v_o}{\sigma_\phi})] \\ &= 1 - I_g(\frac{v_o}{\sigma_\phi}) \\ &= 1 - I_g(\frac{1}{\zeta}) \end{aligned} \quad (13)$$

where $I_g(x) = \int_{-\infty}^x \frac{e^{-t^2/(2\sigma_\phi^2)}}{\sqrt{2\pi}\sigma_\phi} dt$ is a Gaussian integral.

λ is related to $\langle j_z \rangle$ by

$$\lambda = \frac{\langle j_z \rangle}{\sqrt{2}V_v R_v} \quad (14)$$

If we further make the approximation that $\langle j_z/r \rangle = \langle j_z \rangle / \langle r \rangle$, then using Eq. (14) we can write

$$\begin{aligned} v_o &= \langle u_\phi \rangle \\ &= \langle j_z/r \rangle \\ &\sim \langle j_z \rangle / \langle r \rangle \end{aligned}$$

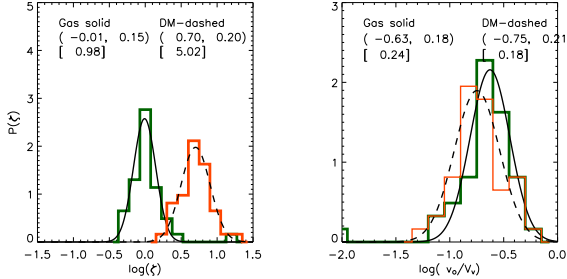


FIG. 12.— Distribution of parameter $\zeta = \frac{\sigma}{v_o}$ and $\frac{v_o}{V_{vir}}$ for a sample of 41 halos at $z=0$. Distributions are roughly log-normal. Gaussian fits are applied and the fit parameters are indicated in upper left and right corners. The position of the peak in normal units is shown below the fit parameters.

$$\begin{aligned} &\sim \frac{\sqrt{2}\lambda/(V_v R_v)}{< r >} \\ &\sim \frac{\sqrt{2}\lambda V_v}{< r/R_v >} \end{aligned} \quad (15)$$

This can be used to express f in terms of λ as shown below

$$\begin{aligned} f &= 1 - I_g\left(\frac{\sqrt{2}\lambda}{< r/R_v > (\sigma_\phi/V_v)}\right) \\ &= 1 - I_g\left(\frac{\sqrt{2}\lambda}{k_r k_\sigma}\right) \end{aligned} \quad (16)$$

where $k_r = < r/R_v >$ and $k_\sigma = (\sigma_\phi/V_v)$ are defined to be two quantities that are constant for a halo. For an NFW halo with concentration parameter c

$$\begin{aligned} k_r &= < r/R_v > \\ &= \frac{\int r \rho(\mathbf{r}) d^3 \mathbf{r}}{\int \rho(\mathbf{r}) d^3 \mathbf{r}} \\ &= \frac{\pi}{4} \frac{[1+c-1/(1+c)-2\ln(1+c)]}{c[1/(1+c)-1+\ln(1+c)]} \\ &= \frac{\pi}{4} f_1(c) \\ &\sim 0.32 \quad \text{for } c = 10.0 \end{aligned} \quad (17)$$

We define

$$\lambda_0 = < k_r > < k_\sigma > / \sqrt{2} \quad (18)$$

then

$$f = 1 - I_g\left(\frac{\lambda}{\lambda_0}\right) \quad (19)$$

Anti-correlation of f with λ

Eq. (19) explains the anti-correlation of f with λ as discussed in Section 3.2.3. Rightmost column in Table 2 and Table 3 lists the values of parameter λ_0 obtained by fitting this equation to the data from simulated halos (Fig. 5). λ_0 as predicted by the toy model can be calculated by using Eq. (18). For this first k_r and k_σ are calculated for each of the halos in the simulation then at any given redshift $< k_r >_{sim}$ and $< k_\sigma >_{sim}$ are calculated by taking the mean over all the halos at that redshift. These values are listed in columns 2 and 4 of the aforementioned tables. λ_0 calculated from these values is listed in column 6. The values of λ_0 predicted by the

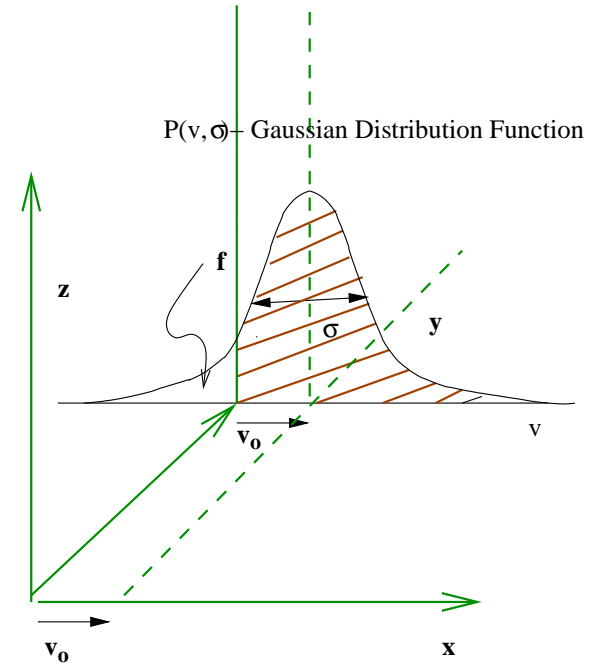


FIG. 13.— Dispersion of ordered velocity v_o by a Gaussian with width σ . $P(v, \sigma) = \frac{1}{\sqrt{2\pi}\sigma} e^{-v^2/(2\sigma^2)}$ is the Gaussian distribution function. A particle has negative angular momentum if $v_{\sigma_\phi} < -v_o$, this is represented by the region under the Gaussian curve which is not shaded.

TABLE 2. k_r , k_σ AND λ_0 FOR GAS

z	$< k_r >$		$< k_\sigma >$		λ_0	
	Sim	ENS	Sim	ENS	pred	Sim
0	0.308	0.315	0.163	-	0.036	0.036
1	0.343	0.349	0.181	-	0.044	0.053
2	0.371	0.373	0.210	-	0.055	0.063
3	0.380	0.390	0.217	-	0.058	0.074
4	0.395	0.402	0.213	-	0.059	0.074

TABLE 3. k_r , k_σ AND λ_0 FOR DARK MATTER

z	$< k_r >$		$< k_\sigma >$		λ_0	
	Sim	ENS	Sim	ENS	Pred	Sim
0	0.308	0.315	0.632	0.654	0.138	0.145
1	0.350	0.349	0.613	0.605	0.152	0.170
2	0.382	0.373	0.595	0.578	0.161	0.178
3	0.398	0.390	0.590	0.561	0.166	0.177
4	0.409	0.402	0.573	0.551	0.166	0.189

NOTE. — Sim: simulations, ENS: calculated theoretically by using Eq. (17) and Eq. (21), c used in calculations is estimated by algorithm given in Eke, Navarro, & Steinmetz (2001) λ_0 Pred: λ_0 as predicted by the toy model Eq. (18), the values of $< k_r >$ and $< k_\sigma >$ used are the ones obtained from simulations, λ_0 Sim: λ_0 as obtained by fitting Eq. (19) to the f vs λ data from simulations (Fig. 5).

toy model have a small offset but otherwise they are in agreement with those obtained from simulations. The increase of λ_0 with redshift can be understood in terms of variation of $\langle k_r \rangle$ and $\langle k_\sigma \rangle$ with redshift. k_r as given by Eq. (17) is a monotonically decreasing function of c . c on the other hand has a dependence on mass, redshift and cosmology given by

$$c = c_{ENS}(\sigma_8, \Gamma, \Omega_\Lambda, \Omega_0, z, M_f, M_0) \quad (20)$$

which can be calculated by means of an algorithm given in Eke, Navarro, & Steinmetz (2001). For calculating $\langle c \rangle$ at a given redshift z we put in Eq. (20) $M_0 = \langle M_v \rangle$ = the mean mass of a halo at that redshift. The predicted ENS values of $\langle k_r \rangle$ are shown in the table, they are in good agreement with those obtained from simulations. For the case here $\langle c \rangle \sim 12.0/(1+z)$ (in agreement with redshift dependence given in Bullock et al. (2001)). This is the cause for increase of $\langle k_r \rangle$ with redshift both for gas and DM. k_σ for DM also depends on c because for DM the one dimensional velocity dispersion is given by $\sigma^2 = (1/3)V_v^2 f_c$, where $f_c \sim 2/3 + (c/21.5)^{0.7}$ (assuming that the velocity distribution is isotropic and homogeneous, see Mo, Mao, & White (1998)).

$$k_\sigma = \frac{\sigma}{V_v} = \sqrt{f_c/3} \sim 0.65 \quad \text{for } c = 10.0 \quad (21)$$

The slight decrease of k_σ with redshifts (Table 3) is again due to increase of $\langle c \rangle$ with redshifts. For DM k_r decreases with c while k_σ increases this makes λ_0 nearly a constant for all the halos at a given redshift and this is one of the reason for the small scatter in f vs λ plots for DM (column 3 Fig. 5). For gas σ_ϕ is not related to V_v and this results in a large scatter seen in its f vs λ plots (column 3 Fig. 5). But k_σ can be written in terms of F_{Tr} as $\langle k_\sigma \rangle \sim \sqrt{F_{Tr}/3}$ and $\langle F_{Tr} \rangle$ increases with redshift (Section 3.3, Fig. 7), explaining the increase of k_σ with redshift shown in Table 2.

It was found in B2001 that standard deviation σ_j of angular momentum for a subsample of N particles for DM scales like

$$\frac{\sigma_j}{J} = \sqrt{1/N + 1/(25\lambda^2 N)} \simeq \frac{0.2}{\lambda\sqrt{N}} \quad (22)$$

In the light of the toy model the error in j , for a sample of N particles at some fiducial radius r , due to Poisson statistics scales as $\sigma_j = \sigma_\phi r / \sqrt{N}$. So

$$\frac{\sigma_j}{j} = \frac{\sigma r}{v_o r \sqrt{N}} = \frac{\zeta}{\sqrt{N}} \quad (23)$$

Comparing Eq. (13) and Eq. (19) $\zeta = \lambda_0 / \lambda$ implying

$$\frac{\sigma_j}{j} = \frac{\lambda_0}{\lambda\sqrt{N}} \quad (24)$$

λ_0 for DM as shown in table above is close to 0.2 which explains the scaling relation observed by B2001.

Distribution of f and its change with redshift

The distribution of λ at any particular redshift is a lognormal distribution which can be specified by parameters λ and σ_λ . By using Eq. (19) we can calculate the distribution of f as shown below

$$P(f)df = \frac{P(\lambda)}{\frac{d}{d\lambda}f(\lambda, \lambda_0)}df \quad (25)$$

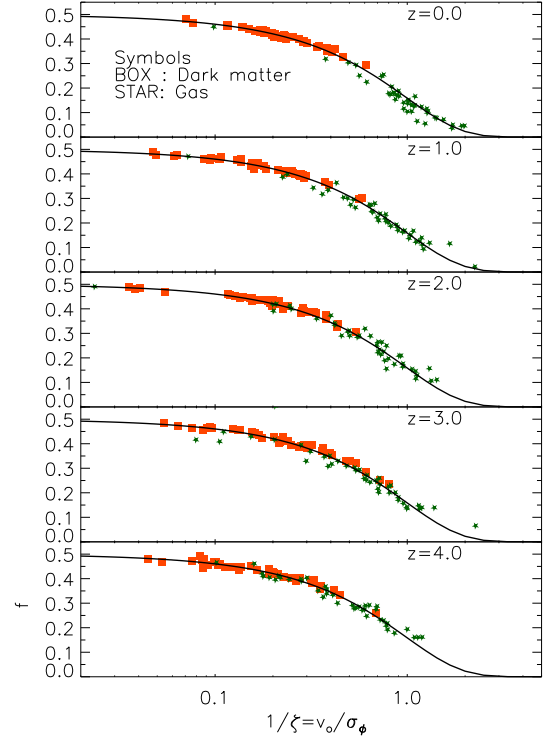


FIG. 14.— Fraction of counter-rotating matter f as a function of $1/\zeta = v_o/\sigma_\phi$ where v_o is the mean tangential velocity and σ_ϕ its dispersion, the two parameters of the GSOV toy model described in Section 4. The solid line is the relationship $f = 1 - I_g(1/\zeta)$ as predicted by the model. Unlike the f vs λ plots where there was a large scatter of points about the theoretical curve for gas (right column Fig. 5) and a free parameter λ_0 was required to fit the different cases, the data points for the f vs $1/\zeta$ plots for both gas and dark matter lie on the same predicted curve and they have a very small scatter.

This predicted formula describes the observed distribution in simulations fairly well. The smooth curve in Fig. 6 is the one predicted by the Eq. (25). $P(\lambda)$ does not have a strong redshift dependence but f is related to λ_0 (Eq. (19)) and λ_0 increases with redshift for gas. This causes the profile of $P(f)$ for gas to shift towards smaller values of f at lower redshifts. For dark matter λ_0 is nearly constant so the profile does not show any significant change. The fact that $\langle f \rangle$ for gas decreases with decrease of redshift is not only due to increasing thermalization of gas as shown in Section 3.3 but is also due to two other factors. $\langle f \rangle$ as given by Eq. (16) depends on $\langle \lambda \rangle$, $\langle k_r \rangle$ and $\langle k_\sigma \rangle$. $\langle \lambda \rangle$ increases, while $\langle k_r \rangle$ and $\langle k_\sigma \rangle$ decreases with decrease in redshift. All of them act in the same direction to decrease $\langle f \rangle$.

f as a function of v_o/σ_ϕ

The relation between f and λ as given by Eq. (19) is an approximate one, the actual relation of f is as given by Eq. (13). Moreover in the plots in Fig. 5 the gas shows a large scatter. So we measure v_o and σ_ϕ for each halo and plot f vs v_o/σ . These are shown as points in Fig. 14. The theoretical prediction of the toy model as given by Eq. (13) is shown as a solid line on the same figure. The large scatter which was seen in f vs λ plots of gas vanishes and moreover there is no free parameter in this relationship.

Calculating the AMDs by utilizing the toy model

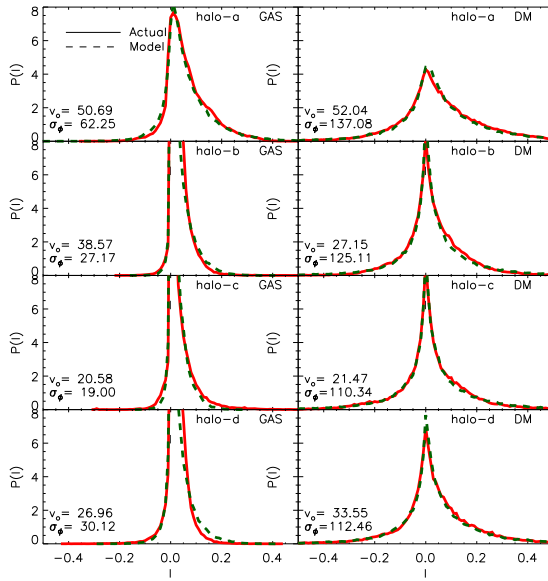


FIG. 15.— Comparison of angular momentum distributions ($P(l)$ vs l) plots where $l = j/(\sqrt{2}R_v V_v)$ obtained from simulations with that of profiles obtained from the Gaussian smearing model (for four different halos same as the ones used in Fig. 11). Solid line: profile from simulations Dashed line: profile generated by smearing model. The parameters v_o and σ_ϕ adopted for generating each of the model profiles is also indicated in each of the panels.

The model can also be used to calculate the AMDs. Consider $m(r)dr$ to be the mass in a cylindrical shell of radius r to $r+dr$. The mean specific angular momentum at this radius is given by $v_o r$. This is smeared by random motion with dispersion σ_ϕ . So the total mass with radius between r to $r+dr$ and specific angular momentum between j to $j+dj$ is given by $\frac{1}{\sqrt{2\pi\sigma_\phi r}} e^{-(j-v_o r)^2/(2(\sigma_\phi r)^2)} dm(r) dr$. Integrating this over r we get the function $m(j)$ which is the mass of halo with specific angular momentum between j to $j+dj$.

$$m(j) dj = \int_0^{R_v} \frac{1}{\sqrt{2\pi\sigma_\phi r}} e^{-(j-v_o r)^2/(2(\sigma_\phi r)^2)} m(r) dr dj \quad (26)$$

For a halo with a given $m(r)$ this integral can be calculated numerically to give the distribution $m(j)$. We instead follow an alternative Monte-Carlo type approach due to its easier implementation. For a given halo once the model parameters v_o and σ are known we calculate the specific angular momentum of each of the particles from equation $j = (v_o + v_{\sigma_\phi})r$ where v_{σ_ϕ} is drawn from a Gaussian distribution of dispersion σ . In Fig. 15 we have plotted the angular momentum distributions obtained by the above procedure along with the AMDs obtained from simulations. They are very similar.

5. GENERALIZED PROFILES BASED ON GAMMA DISTRIBUTION

The various AMDs that have been analyzed in the previous sections can be well described by an analytical function that depends on just one parameter. The functional form for the differential distribution is based on the gamma distribution and reads

$$P(j) = \frac{1}{j_d^\alpha \Gamma(\alpha)} (j)^{\alpha-1} e^{-j/j_d} \quad (27)$$

Since it is normalized it satisfies $\int_0^\infty P(j) dj = 1$. Using the fact that $\int_0^\infty j P(j) dj = J/M = j_{tot} = \sqrt{2}R_{vir}V_{vir}\lambda$ we get

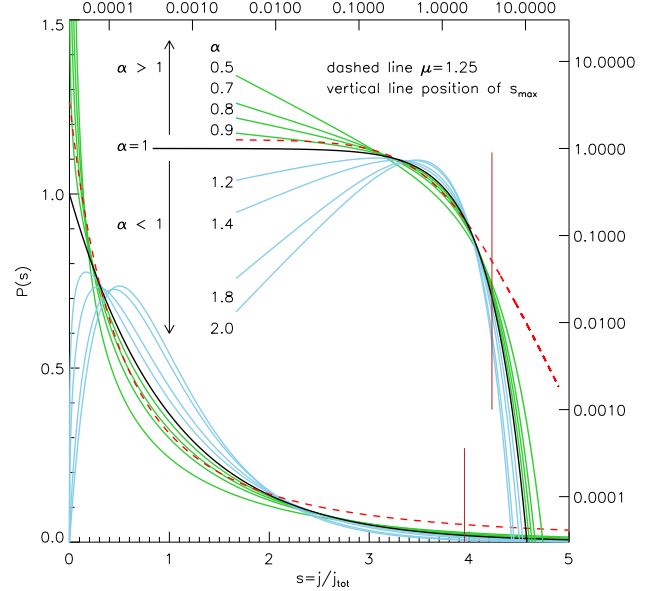


FIG. 16.— The differential distribution of specific angular momentum for various values of α . Both linear and log-log plots are shown. The dashed line corresponds to universal profile of Bullock et al. (2001) with $\mu = 1.25$ and the vertical line shows the position of s_{max} for it. α is sensitive to the slope in the inner regions. $\alpha = 1$ marks the transition from a distribution that diverges as $s \rightarrow 0$ ($\alpha < 1$) to the one that dips to zero ($\alpha > 1$).

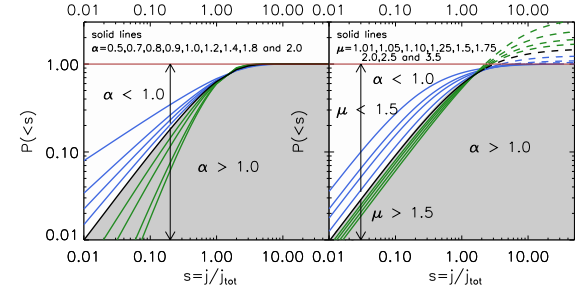


FIG. 17.— The cumulative distribution $P(< s)$ of specific angular momentum $s = j/j_{tot}$ for various values of α (left) and μ (right). The shaded area separates the region with values of $\alpha > 1$ from those with $\alpha < 1$ (unshaded area), in both the plots. The $\alpha = 1$ curve roughly corresponds to curve with $\mu = 1.5$. The functional form of μ profiles can extend beyond $P(< s) = 1$, this is shown as dashed lines. The profiles are truncated at $s = s_{max}$ the point where $P(< s) = 1$. For α profiles $P(< s)$ is always less than 1 and it asymptotically approaches 1 for large values of s . α and μ measure slightly different aspects of the shape. μ curves are a power law with slope of 1 for small s and the value of μ is a measure of the point where the bend takes place. α on the other hand is sensitive to the slope of the curve for small s .

$$j_d = \frac{j_{tot}}{\alpha} \quad (28)$$

This makes the distribution a one-parameter fit. We choose α as the parameter as its effect is easy to understand on physical terms. The differential distribution can be integrated to get the cumulative distribution as shown below.

$$P(< j) = \frac{M(< j)}{M_v} = \int_0^j P(j) dj = \gamma(\alpha, j/j_d) \quad (29)$$

where γ is the Incomplete Gamma function. Writing in terms of $s = j/j_{tot}$ and replacing j_d we get

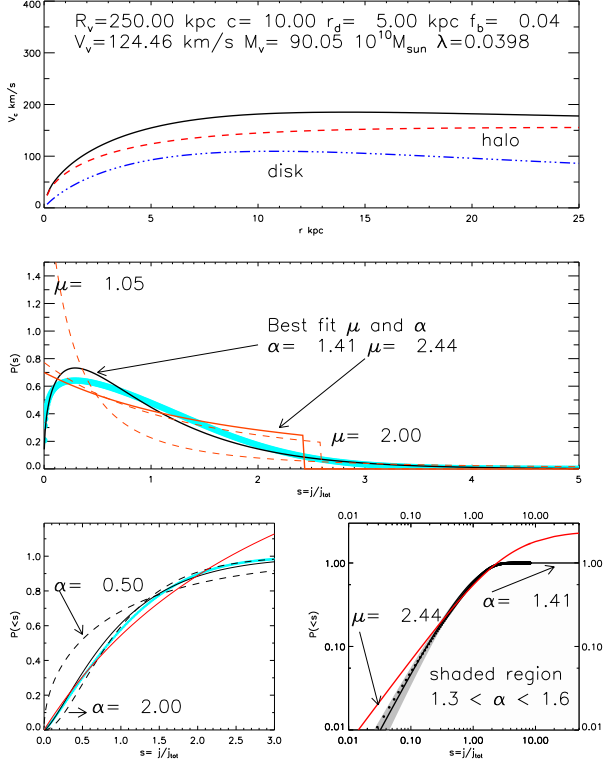


FIG. 18.— The AMD of an exponential disk embedded in an NFW halo. Rotation curves are calculated by taking the adiabatic contraction of the halo and the flattened geometry of the disk into account. The thick light line (cyan) are the data points corresponding to AMD obtained from the model. A value of $\alpha = 1.41$ seems to fit the model AMD (thin dark; black). μ profiles are not very suitable for describing the model profiles. The best fit μ curve is shown as solid line (thin semi dark; red) and also for reference curves with $\mu = 1.05$ and $\mu = 2.0$ are also shown as dashed lines in the second panel. In lower-left panel we plot the cumulative distributions, the solid lines are the curves with best fit values of α and μ . The dashed lines here are for curves with $\alpha = 0.5$ and $\alpha = 2.0$. In lower-right panel the shaded strip corresponds to the region where $1.3 < \alpha < 1.6$, which is the expected range of values for model galaxies with $2 < c < 20$ ($r_d < 7\text{kpc}$ and $R_v > 200\text{kpc}$). The dots are the AMD of the model.

$$P(< s) = \gamma(\alpha, \alpha s) \quad (30)$$

Fig. 16 shows $P(s)$ vs s plots for various values of α in both linear and logarithmic plots. For $s \ll 1/\alpha$, $P(s)$ is a power law with slope $\alpha - 1$. So for $\alpha > 1$ $P(s)$ goes to zero as $s \rightarrow 0$, and this gives rise to a dip which is similar to the AMDs of observed dwarf galaxies as shown in BBS01. For $\alpha < 1$ the profiles diverge as $s \rightarrow 0$ similar to AMDs seen in simulations.

Fig. 17 illustrates the effect of α on the shape of $P(< s)$ vs s plots, for reference we also illustrate the effect of varying μ (B2001) on the shape of the profiles.

5.1. What kind of AMD do spiral galaxies have?

AMDs of observed dwarf galaxies as illustrated in BBS01 are found to have a dip at low s which suggests that they can be fit with a profile having $\alpha > 1$. The simple case of an exponential disk rotating in an isothermal halo ($\rho(r) \propto 1/r^2$) with flat rotation curve can be calculated analytically and it gives a profile with a value of $\alpha = 2$. To investigate the AMDs of disk galaxies in more detail and to find out the range of values of α that they satisfy we create a model in which an exponential disk of mass fraction f_d and scale length r_d is embedded in an

NFW DM halo of virial radius R_v and concentration parameter c , similar to analysis by Mo, Mao, & White (1998). The disk mass fraction is defined as $f_d = M_{disk}/(\Omega_b M_v / \Omega_m)$. For calculating the rotation curve we take into account the adiabatic contraction of the halo and also the flattened geometry of the disk. So the input parameters for the model are R_v , r_d , f_d and c . Fig. 18 shows a typical AMD obtained by this model.

The profile is very similar to that observed by BBS01. It can also be seen from the figure that the μ profiles are very different from the AMD of model galaxies. For higher values of μ (about 2) they can be an approximate fit but still they have a distinct core and tail excess. They do not show the characteristic dip at low j as shown by models and also the tail has an abrupt truncation whereas the models show a smooth extended distribution. So a μ profile even with higher values of μ does not describe the AMD of real galaxies. The generalized profile described in Section 5 provides a good fit to these model profiles. For realistic values of the model parameters as shown in Fig. 18 we get $\alpha \sim 1.4$. α is a strong function of concentration parameter c but only weakly related to r_d , R_v and f_d (keeping other parameters fixed). For lower values of f_d the fits get more and more accurate. α increases from 1.30 for $c = 2$ to 1.6 for $c = 20$ (with $r_d < 7\text{kpc}$ and $R_v > 200\text{kpc}$). We assume $1.3 < \alpha < 1.6$ as the typical range of values expected for real galaxies.

6. TECHNIQUES TO MEASURE THE ANGULAR MOMENTUM DISTRIBUTION OF HALOS IN SIMULATIONS

In this section we first describe two different methods to measure the AMDs in halos followed by analysis of AMDs obtained by each of these methods. As described earlier the velocities given by simulations are of two types. The velocity of an SPH particle (gas) refers to the streaming velocity u while the velocity of a DM particle samples the actual microscopic velocity $v = u + w$, where w is the random motion. One method to measure the angular momentum distribution is to take the angular momentum of each particle and plot its distribution (**particle method**). This inevitably gives a negative tail resulting in a significant fraction of matter with negative AM. For gas we find it to be between 4% to 48% with a mean of about 15% while for DM it is between 30% to 48% with a mean of 41%. This not only makes the interpretation of AMD obtained by the particle method difficult but also the comparison between the AMDs of gas and DM. To make both the components come to the same footing we can either **broaden** the velocities of gas particles or **smooth** the velocities of both gas and DM particles over a fixed number of neighbors. However, even smoothening the velocities over 1000 neighbors is not enough to suppress the negative angular momentum tail.

B2001 obtain the AMD by dividing the halo into cells and then calculating the angular momentum by averaging over all particles in the cell (**cell method**). These cells are then used to plot the cumulative distribution. In the particle method described above it is possible to derive both the differential and cumulative profiles while in the cell method only latter is possible owing to the small number of cells, typically around 60. Furthermore, the cells are assumed to have a spherically symmetric geometry. Each cell covers a full 2π range in ϕ and they span the range of $(r/R_v, \sin\theta)$ from $(0,0)$ to $(1,1)$. The radial shells are spaced such that each of them contains the same number of particles. The shells are then divided into 3 azimuthal cells of equal volume between $\sin\theta = 0$ and 1. Positions with same $rsin\theta$ above and below the plane belong to same cell. For our calculations we divide the halo into

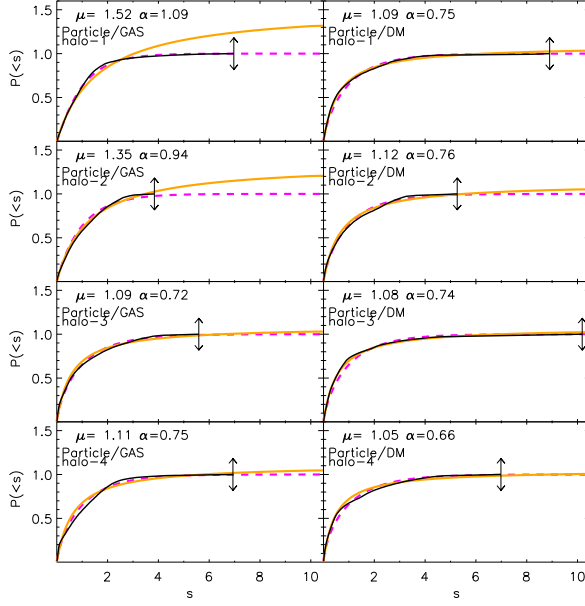


FIG. 19.— The cumulative angular momentum distribution for 6 different halos obtained by the particle method (dark solid line). For each halo, distributions for both gas and dark matter are shown. The best fit α and μ values are also labeled. Light solid line (orange): best fit μ profile constant λ fit. Dashed line (magenta): best fit α profile. Up down arrows mark the point with maximum value of s . The profiles have a smooth truncation the slope in outer parts gradually goes to zero. s_{max} is higher than that obtained by cell method.

60 cells with approximately constant number of particles in each of them. We call this method **symmetrical cell method**. The symmetrical cell method is more effective in reducing the negative AM material compared to particle method. However the resulting AMD might be biased if the system is not axis symmetric. We therefore repeat the analysis with a modified scheme which is free from any inherent symmetry. We divide the halo into 4 radial shells with the n th shell containing $2n^2$ particle (2, 8, 18 and 32). Each shell is divided into n polar zones denoted by l . Each l region is divided into $2l+1$ azimuthal zones. Finally regions above and below the z plane belong to different cells. The radial and polar divisions are done such that each cell contains a constant number of particles. We refer to this method as **normal cell method**.

6.1. Analysis by cell method and Bullock profiles

In B2001 cumulative AMDs were calculated by the symmetrical cell method for DM halos and a universal profile with shape parameter μ was shown to fit the data. The distribution of μ was found to satisfy a log-normal distribution with $\langle \log_{10}(\mu-1) \rangle = -0.6$ and $\sigma = 0.4$. Our simulations reproduce these findings as shown in Fig. 23 (second row). Chen & Jing (2002, henceforth CJ02) have also obtained similar results except the fraction of cells with negative AM is higher than in B2001. B2001 found that 5% of halos have $f > 0.1$ while CJ02 found it to be 40%. Chen, Jing, & Yoshikawa (2003, henceforth CJ03) have also analyzed the AMDs for both gas and DM components. They found that μ is higher for gas than that for DM and also that f is lower for gas. Results of our simulations agree quite well with the findings of CJ02 and CJ03. We find that for DM $f > 0.1$ for 33% of halo while for gas $f > 0.1$ for 9% of halos. $\langle f \rangle$ for DM is $\sim 9\%$ while for gas it is $\sim 3\%$. We also find μ to be higher for gas compared

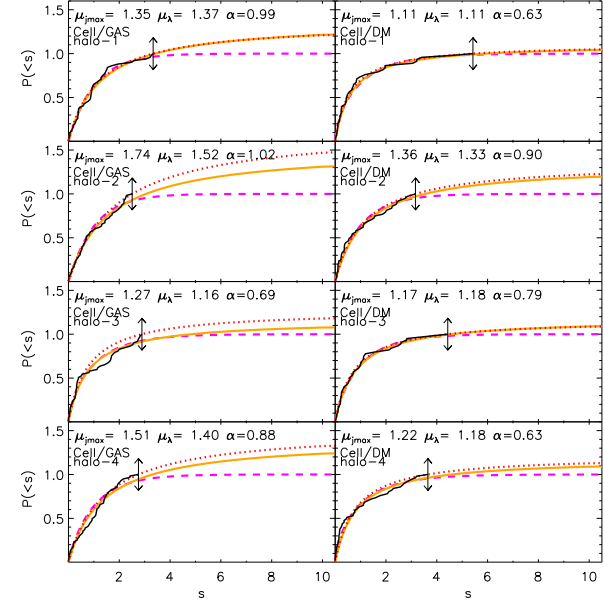


FIG. 20.— The cumulative angular momentum distribution for 6 different halos obtained by symmetrical cell method (dark solid line). For each halo, distributions for both gas and dark matter are shown. The best fit α and μ values are also labeled. Light solid line (orange): best fit μ profile constant λ fit. Dotted line (red): best fit μ profile constant j_{max} fit. Dashed line (magenta): best fit α profile. Up down arrows mark the point with maximum value of s . The constant j_{max} fits always pass through the point with maximum s while the constant λ and α profiles in general do not. The profiles tend to have an abrupt truncation, which means that at $s = s_{max}$ the slope is significant.

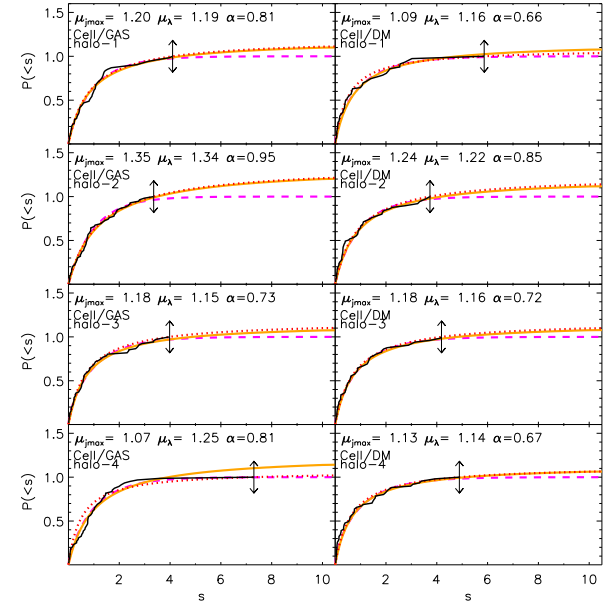


FIG. 21.— The cumulative angular momentum distribution for 6 different halos obtained by normal cell method free from any symmetry restrictions (dark solid line). For each halo, distributions for both gas and dark matter are shown. The best fit α and μ values are also labeled. Light solid line (orange): best fit μ profile constant λ fit. Dotted line (red): best fit μ profile constant j_{max} fit. Dashed line (magenta): best fit α profile. Up down arrows mark the point with maximum value of s . The profiles end at higher values of s and they also tend to have smoother truncation compared to profiles obtained by the symmetrical cell method. They are more similar to the profiles obtained by the particle method.

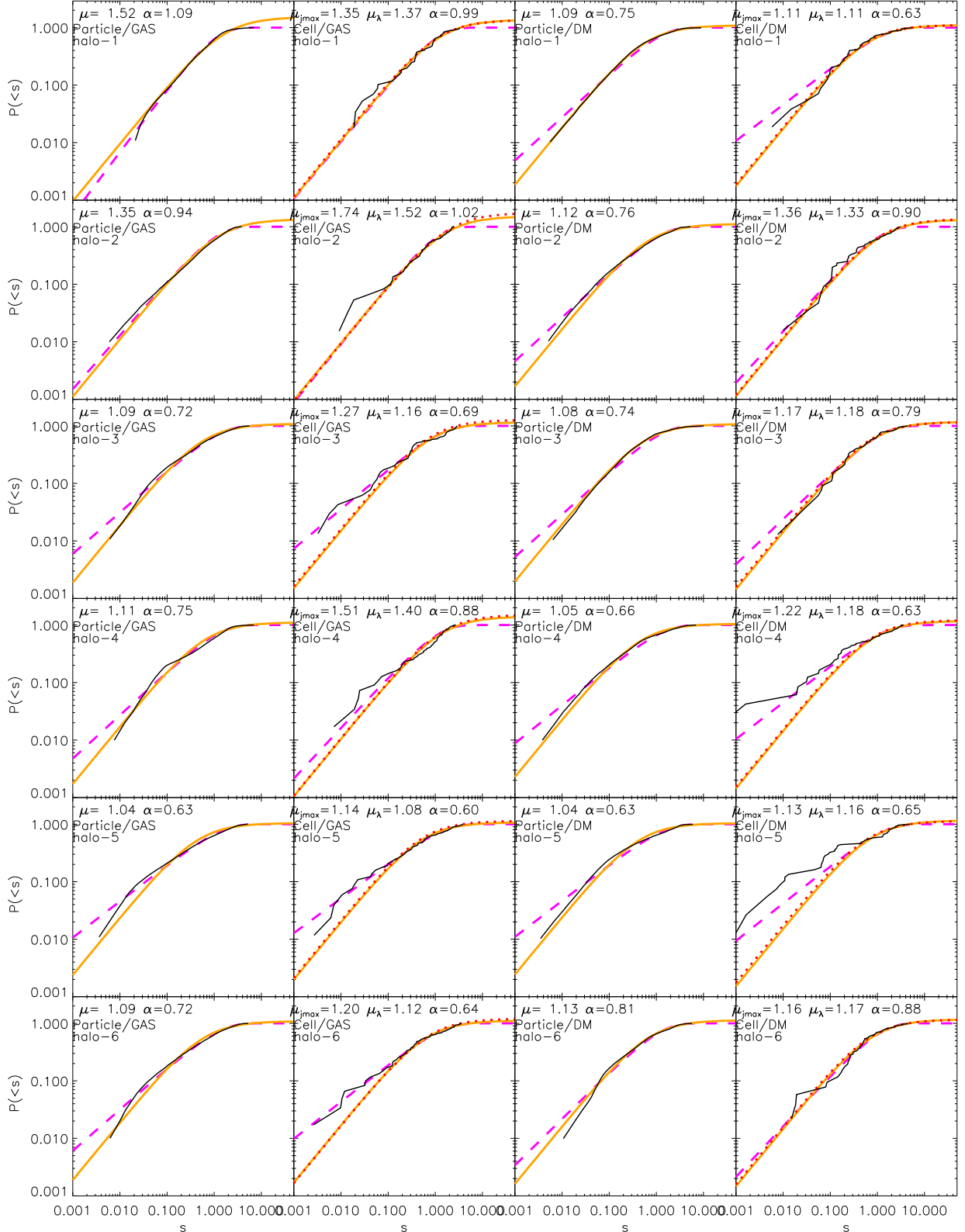


FIG. 22.— The cumulative angular momentum distribution for 6 different halos (dark solid line). Each row corresponds to a particular halo. Profiles of each halo both for gas and dark matter by particle and as well as symmetrical cell method are shown. Also are labeled the best fit α and μ values. Light solid line (orange): best fit μ profile constant λ fit. Dotted line (red): best fit μ profile constant j_{max} fit. Dashed line (magenta): best fit α profile. The subscript to μ denotes if it is a constant λ or a constant j_{max} fit. For particle method the μ profiles are generated by constant λ fits only.

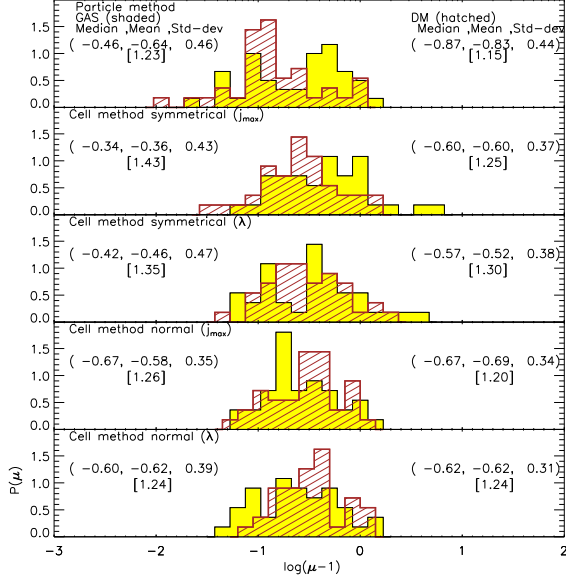


FIG. 23.— Distribution of shape parameter μ for angular momentum distributions obtained by various different methods and fitting techniques. Median, mean and standard deviation of $\log(\mu-1)$ is also indicated for each case, and below it corresponding μ value is shown. For gas the constant λ fits have lower mean and higher width compared to constant j_{\max} fits. On the other hand for DM the mean increases. Same trend is observed in analysis with normal cells. In comparison with symmetrical cells the normal cells give a lower mean and width for the μ distributions. The particle method gives even lower mean but the widths are maximum.

to DM (second panel Fig. 23) by using the same methods for analysis as done by above authors.

However, we observed that the μ values obtained from fitting $M(< j)$ vs j data are sensitive to the fitting procedure and error bars used. In fact two techniques can be used to fit μ profiles each giving slightly different results. The analytic function for the μ profiles is given by

$$\frac{M(< j)}{M_v} = P(< j) = \frac{\mu j}{j_0 + j} \quad (31)$$

j_0 can be written in terms of λ and μ as

$$j_0 = \frac{j_{\text{tot}}}{b(\mu)} = \frac{\sqrt{2}V_v R_v \lambda}{b(\mu)} \quad (32)$$

where $b(\mu) = -\mu \ln(1 - \mu^{-1}) - 1$. This makes the μ profiles a one parameter fit for a halo with a given λ .

$$P(< j) = \frac{\mu j}{j_0(\mu, \lambda) + j} \quad (33)$$

$$P(< s) = \frac{\mu s}{1/b(\mu) + s} \quad (34)$$

We call this the **constant λ fits**. Alternatively the μ profiles have an implicit maximum specific angular momentum $j_{\max} = j_0/(\mu-1)$. Writing in terms of j/j_{\max}

$$P(< j) = \frac{\mu j/j_{\max}}{(\mu-1) + j/j_{\max}} \quad (35)$$

For a given halo in simulations j_{\max} is the specific AM of the cell having maximum specific AM. This is again a one parameter fit which we call **constant j_{\max} fits**.

In B2001 it was shown that for DM the error bars on values of j for DM can be approximated by $\sigma_j = 0.2/(\lambda\sqrt{N})$. The

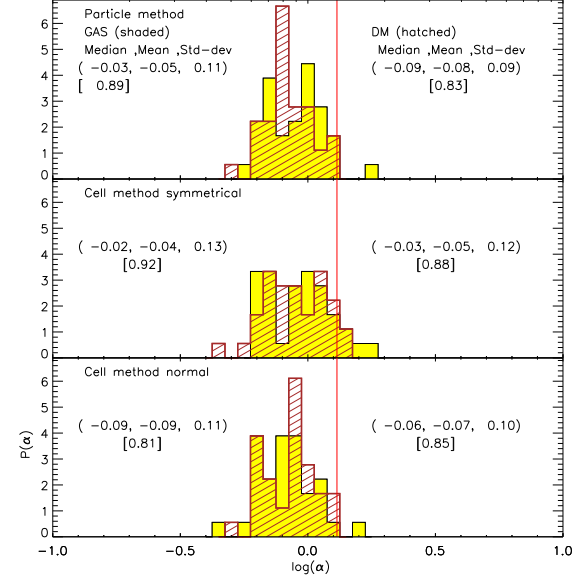


FIG. 24.— Distribution of shape parameter α for angular momentum distributions obtained by the particle and by the cell method. Median, mean and standard deviation of $\log(\alpha)$ is also indicated for each case, and below it corresponding α value is shown. The vertical line corresponds to $\alpha = 1.3$. The normal cell method gives lower values of mean and width for both gas and DM components compared to symmetrical cell. The same trend is observed for particle method except that the mean value for gas increases.

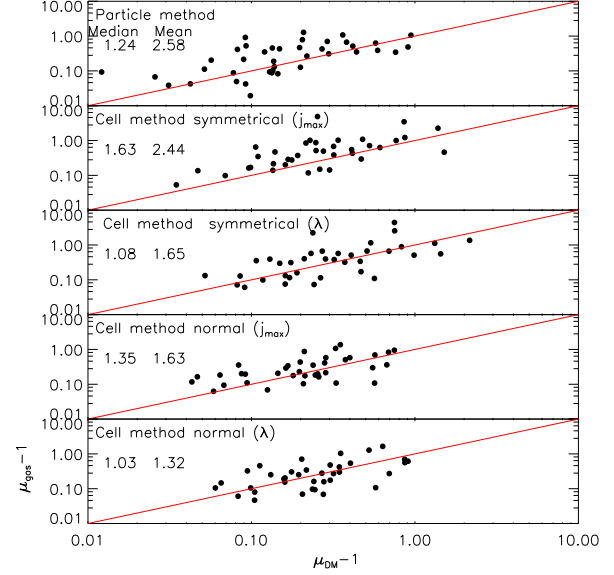


FIG. 25.— $\mu_{\text{Gas}} - 1$ vs $\mu_{\text{DM}} - 1$ for various different techniques. Median and mean of $(\mu_{\text{Gas}} - 1)/(\mu_{\text{DM}} - 1)$ are also labeled on each of the plots. The straight line shown in the plot corresponds to the relation $\mu_{\text{Gas}} = \mu_{\text{DM}}$. Particle method and constant j_{\max} fits have $\mu_{\text{Gas}} > \mu_{\text{DM}}$ but constant λ fits do not show any significant bias.

velocity dispersions are in general not homogeneous throughout the halo. CJ03 therefore base their analysis on error bars estimated by $\sigma_j = v_c(r)r/\sqrt{N}$. However, gas particles have a much smaller velocity dispersion. We therefore use a scheme in which the error are estimated by $\sigma_j = j_{\text{std-dev}}/\sqrt{N}$, where $j_{\text{std-dev}}^2 = \langle (j - \langle j \rangle)^2 \rangle$ is the standard deviation calculated over the particles in the cell. For the cumulative distribution

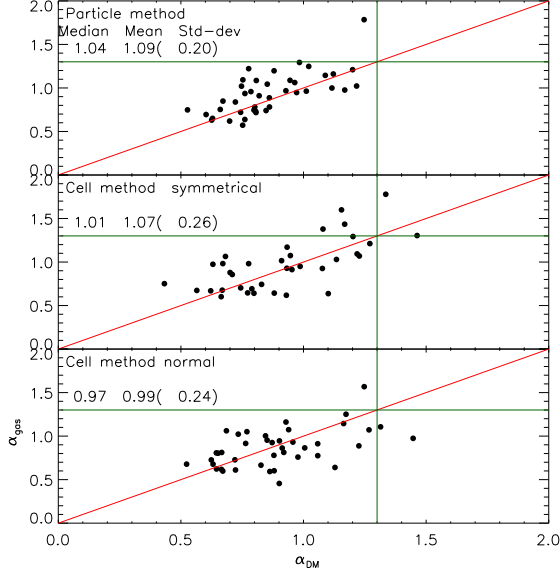


FIG. 26.— α_{Gas} vs α_{DM} for various different techniques. Median, mean and standard deviation of $(\alpha_{Gas}/\alpha_{DM})$ are also labeled on each of the plots. The straight line shown in the plot corresponds to the relation $\alpha_{Gas} = \alpha_{DM}$. In particle method we see $\alpha_{Gas} > \alpha_{DM}$ but cell method does not show such a bias. The two vertical and horizontal lines correspond to $\alpha = 1.3$ and there are very few halos that lie above these lines (except for the middle panel which has a few).

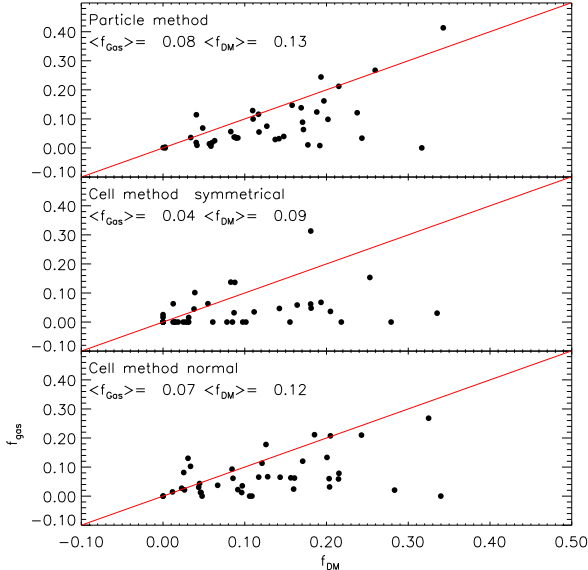


FIG. 27.— Comparison of parameters f_{Gas} and f_{DM} for various different techniques. $\langle f_{Gas} \rangle$ and $\langle f_{DM} \rangle$ are also shown. The distribution for normal cell method is very similar to that of particle method. In symmetrical cell method f is in general much lower and for gas a significant number of the halos have $f = 0$.

$P(< j)$ vs j , σ_j gives the error along j -axis. We estimate the error along $P_{<}$ axis by $\sigma_{P_{<}} = (dP_{<}/dj)\sigma_j$. To calculate $dP_{<}/dj$ we first fit the data with a μ or α profile and then use this value of μ or α to calculate $dP_{<}/dj$. AMDs obtained by both particle and cell methods along with corresponding μ and α fits are shown in Fig. 19, Fig. 20, Fig. 21 and Fig. 22.

We find that for constant j_{max} fits $\mu_{gas} > \mu_{DM}$ in agreement

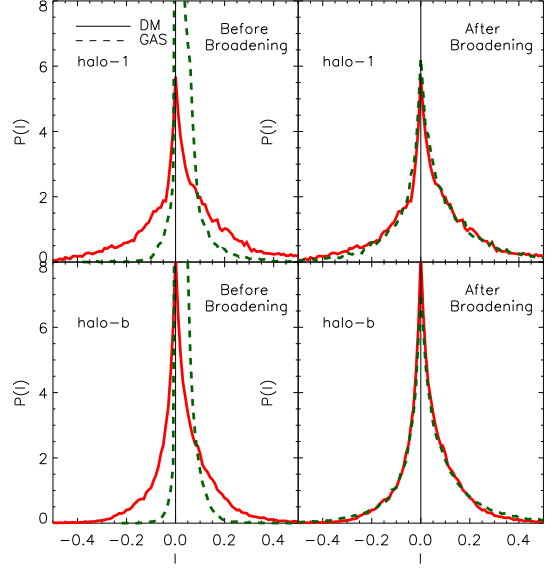


FIG. 28.— Effect of broadening the velocities on the distribution of angular momentum for two different halos. After broadening the angular momentum distribution of gas is very similar to that of dark matter.

with CJ03 (Fig. 23 and Fig. 25, second row). The distribution of $\log(\mu - 1)$ can be roughly fit by a Gaussian and the fit parameters for DM are similar to those in B2001. For constant λ fits however, we find that μ_{gas} is nearly same as μ_{DM} . The reason for the discrepancy is that the constant j_{max} fits are constrained by construction to satisfy $P(< j) = 1$ at $j = j_{max}$, so the error in the value of j_{max} is not taken into account in the fitting procedure. Moreover the fits are not constrained to satisfy Eq. (32). For constant λ fits and also the α fits this is not the case, the curves do not necessarily truncate at $j = j_{max}$: they may extend to $j > j_{max}$ or may already stop at $j < j_{max}$ (Fig. 20). There is a systematic trend such that for cases where μ is high (in constant j_{max} fits), the constant λ fits truncate at $j > j_{max}$, resulting in a lower value of μ . The DM does not have high values of μ so it is relatively unaffected while gas has relatively high values of μ and is significantly affected. In other words, the effect that $\mu_{gas} > \mu_{DM}$ is diminished to a large extent in the constant λ fits. The distributions of α_{gas} and α_{DM} also show only a mild bias, (Fig. 24 second row). About 20% of halos had $\alpha > 1.3$ but out of these for 10% of halos the fits were poor so they were rejected. After correction only 10% of halos have $\alpha > 1.3$ for gas, while for DM the percentage is about 5% (Fig. 26).

Changing the geometry of the cells changes the distributions of μ and α slightly. The peak position and width of the distributions are both reduced. A smaller percentage of halos have $\alpha > 1.3$. We address the reason for these results in the next section.

6.2. Analysis by particle method

Is broadening technique suitable for comparing AMD of gas and DM?

It was shown in vB2002 that the AM profiles of gas and DM are remarkably similar, if not identical, when the velocities of gas were broadened by their microscopic thermal motion (Fig. 28). However, if the shape of the profiles after broadening is determined primarily by the value of σ and is thus insen-

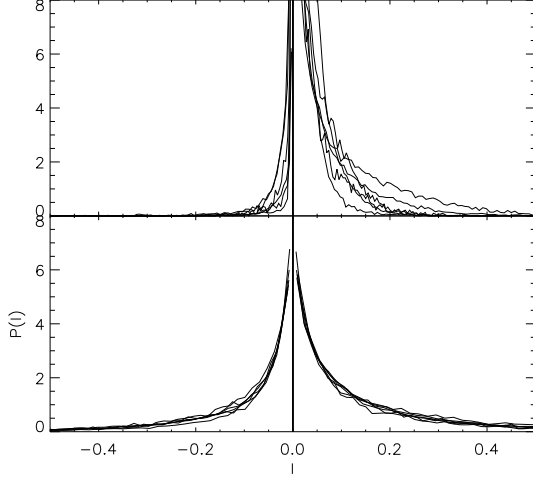


FIG. 29.— Angular momentum distribution of gas of six different halos before broadening (**top panel**) and after broadening their velocities with $\sigma = 160.1 \text{ km s}^{-1}$ (isothermal broadening) (**lower panel**). After broadening all the different distributions are similar so broadening is not a very reliable technique for making comparison between the distributions of gas and DM.

sitive to the original shape, then different profiles can be made to look similar by broadening with same σ . We demonstrate this in Fig. 29 where we broaden the streaming velocities of 6 halos, each with a unique AMD, with same velocity dispersion $\sigma = 160.1 \text{ km s}^{-1}$. Although the initial profiles were quite different, the profiles after broadening are very similar. We conclude that thermal broadening masks out the uniqueness of un-broadened AMDs and hence is not a suitable technique for making comparisons.

Angular momentum distributions after smoothening

Rather than broadening we consider smoothening of the DM velocities as the superior procedure, i.e. we extract streaming velocity u from the given velocity v and then compare their AMD with that of gas. Increasing the numbers of neighbors N_{ngb} , over which the smoothening is applied, will decrease f but then the region over which averaging is done eventually becomes too large and any significant information is lost. Furthermore, particles close to the rotation axis suffer an apparent loss of AM due to a geometrical effect: $\langle v_x \rangle$ and $\langle v_y \rangle$ in the inner region are zero for a symmetric rotating system aligned along z axis. Alternatively we may smooth the AM instead (the halo should be centered before smoothening). In this case we encounter the following problem: Particles close to the axis and in a conical region around it get enhanced in AM while those along the equator suffer a loss in AM due to the existence of a strong density gradient. A spherical volume around such a typical particle has more neighbors towards the symmetry axis with lower AM than away from it, so the smoothed AM which has a radial dependence given by $j(r) = v_o r$, is lower close to the axis. This effect was not prominent when the smoothening was done on velocities because the velocity does not exhibit a strong radial dependence ($v(r) \sim v_o$). This suggests that a better method would be to smooth the velocities in cylindrical co-ordinates. For our analysis here we use the technique of smoothening the angular momentum only and we choose the number of neighbors to be 400. Instead of an SPH type kernel we use a simple step function, which is equivalent to taking the mean over the

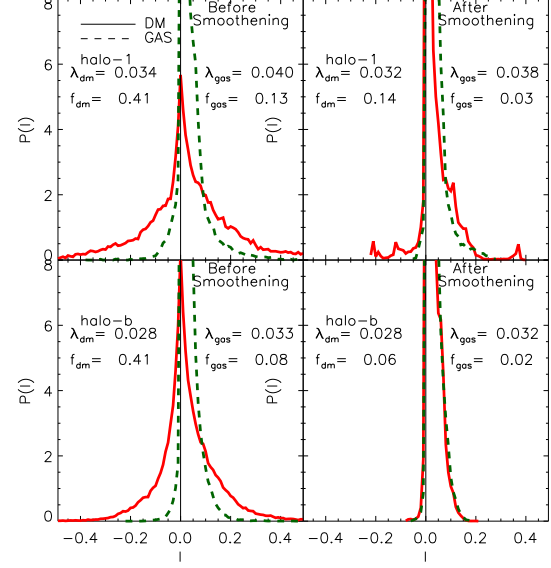


FIG. 30.— Effect of smoothening on the angular momentum distributions of two different halos (same as in Fig. 28). The angular momentum of both gas and dark matter is smoothed by taking mean over 400 neighbors. For some halos after smoothening the gas and DM profiles are similar while for others they are different, one of the reasons for this is that the λ and f are not same for gas and DM.

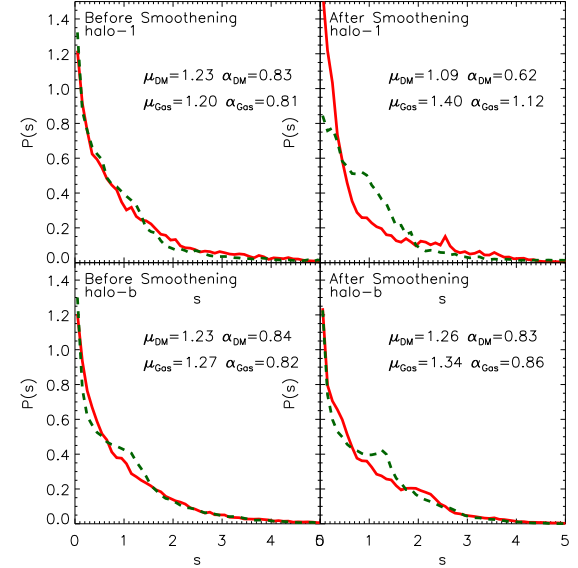


FIG. 31.— Effect of smoothening on the $P(s)$ vs s plots of two different halos (same as in Fig. 28). The angular momentum of both gas and dark matter is smoothed by taking mean over 400 neighbors. For the halo in the lower panel, the gas and DM profiles after smoothening are similar but for the other halo they are different.

neighbors. This makes it easier to make comparisons with the cell method and is also more effective in reducing f .

In (Fig. 30) the effect of smoothening on the distributions of angular momentum is shown. For some halos the profiles of gas and DM are similar after smoothening and for some they are different. This kind of comparison is not very useful because the shape of $P(l)$ vs l plots depends on λ and f . So a good agreement may merely reflect that the λ and f are

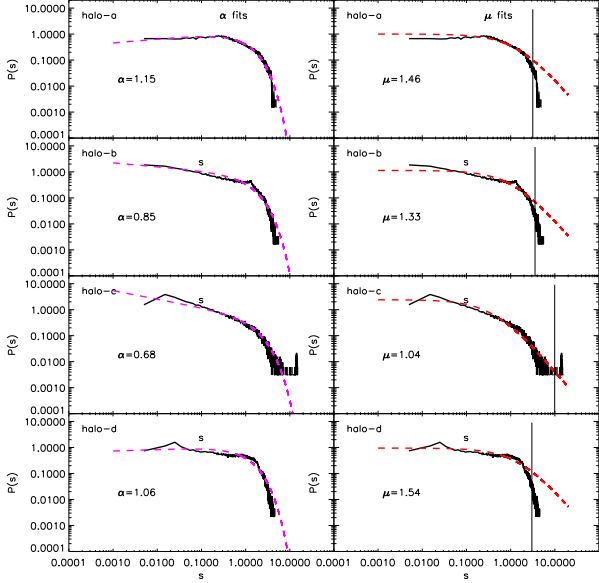


FIG. 32.— A comparison of μ and α fits applied to angular momentum distributions of the gas obtained by the particle method. The vertical line in plots on the right indicate the truncation point s_{max} of μ profiles. The solid lines are the data obtained from simulation and the dashed lines are the best fit α (left) and μ (right) profiles. In outer parts the actual profiles are steeper than $1/s^2$ (the expected asymptotic form of μ profiles).

similar for gas and DM. Moreover λ and f are in general not same for gas and DM, this makes the interpretations of these plots even more difficult.

So to make a comparison first we need to take out the dependence on λ and f which can be done by plotting $P(s)$ vs s for the positive tails of gas and DM and then comparing the best fit values of μ or α . This is shown in Fig. 31.

Analysis of smoothed profiles

We bin the smoothed profiles such that each bin contains $N_{halo}/100$ particles. For calculating the error bars we use the same technique as described earlier in the case of the cell method, with the exception that we assume $\sigma_j/j = \langle \zeta \rangle / \sqrt{N}$. For DM $\langle \zeta \rangle = 5$ and with $N = 400$ this gives a value of 0.25. For gas $\langle \zeta \rangle = 1$ and this gives a value of 0.04. The smoothed profiles can be fit by both Bullock μ profiles (only constant λ fits are used) and the generalized α profiles Fig. 31. $P(s)$ vs s differential plots in Fig. 32 show that that the Bullock profiles are shallower for large s , i.e. the actual AMDs are steeper than $1/s^2$ in outer parts. The particle profiles do not truncate abruptly like in the cell method, the slope gradually goes to zero. The α profiles provide better fit to the particle profiles in outer regions.

The μ and α values obtained by particle method are also larger for gas as compared to that of DM (Fig. 25 and Fig. 26). $\log(\mu-1)$ and $\log(\alpha)$ distributions are roughly Gaussian. The mean, median and standard deviation are shown in Fig. 23 and Fig. 24. $\alpha > 1.3$ for about 2% of gas halos while none of the DM halos have $\alpha > 1.3$. Even after smoothening with same number of neighbors in particle method f on average is greater for DM (13%) than for gas (8%). Similar effect is also seen in cell method where the cell size used is same for both DM and gas Fig. 27.

Effect of spherical and symmetric cell geometry

A comparison of results of particle method with that of symmetrical cell method show that μ (constant λ fits) and α are higher for symmetrical cell method. μ specifically is higher because s_{max} to which it is directly related is about 1.5–2.0 times higher in particle method than in symmetrical cell method (Fig. 19, Fig. 20) although the number of neighbors in particle method is approximately the same as the number of particles in each cell. f is also significantly lower in symmetrical cell method than in particle method (Fig. 27). Since smoothening is a local effect whereas cell averaging is not due to its spherical and symmetric construction. So a blob of negative AM or higher AM material will retain its character when smoothed but will be averaged out in cell method over regions that are not necessarily local. Both methods will deliver identical results only in the case where the system is symmetrical. Any deviation from symmetry, in the symmetrical cell method has the effect of lowering the low AM material by mixing it with high AM one and vice versa. So both f and s_{max} are lower in symmetrical cell method. α does not depend upon s_{max} but is only affected by the lowering of low AM material and this effect is not very strong so it shows only a slight change.

These arguments also imply that the results of normal cell method should be very similar to particle method. This is indeed the case as can be seen in Fig. 27 where distribution of f for normal cell method is very similar to particle method. The distribution of α and μ parameter for particle method is also closer to normal cell method than the symmetrical cell method as shown in Fig. 26. In spite of the similarities there are subtle differences specially for gas whose $\langle \log(\alpha) \rangle$ is much lower for the case of normal cell method. This discrepancy may be because the number of particles in the normal cell is not fixed for all halos like in particle method for which the number is 400. Compared to normal cell method the particle method has slightly lower values of μ because their s_{max} is slightly higher and this is because AM is a monotonically increasing function of radius and for a cell of finite radial thickness the average AM of the cell will always be less than the maximum AM of particles in it.

Measuring the spatial asymmetry of angular momentum distribution within a halo

The above discussion suggests that both gas and DM should have significant asymmetry. We verify this as follows: We measure the asymmetry by dividing the halo into cells as described earlier but this time each radial shell is also divided into 6 azimuthal zones and 3 θ zones. Then we measure the z component of angular momentum vector $j(r)$ and $j(r')$ for a pair of cells with opposite parity situated at \mathbf{r} and \mathbf{r}' where $\mathbf{r}' = -\mathbf{r}$. Symmetry of j distribution within a halo is given by

$$S_j = \left\langle \frac{|j(r) + j(r')|^2 - |j(r) - j(r')|^2}{|j(r) + j(r')|^2 + |j(r) - j(r')|^2} \right\rangle_{\text{all cells}} \quad (36)$$

$$= \left\langle \frac{2j(r)j(r')}{j^2(r) + j^2(r')} \right\rangle_{\text{all cells}}$$

S_j can vary from -1 (perfectly anti-symmetric system) to 1 (perfectly symmetric system). An asymmetry as high as $j(r) = 2j(r')$ corresponds to S_j of only 0.8. $\langle S_j \rangle$, the mean over all halos, is found to be 0.78 for DM and 0.83 for gas. So in halos both gas and DM have significant asymmetry as expected. DM in fact is more asymmetrically distributed than gas.

TABLE 4. COMPARISON OF χ^2 FOR μ AND α FITS

	Cell method ^a		Particle method	
	DM	GAS	DM	GAS
median(χ_α^2/χ_μ^2)	0.78	1.31	1.47	0.92
median($\frac{\chi_\alpha^2 - \chi_\mu^2}{\chi_\mu \chi_\alpha}$)	-0.25	0.27	0.39	-0.08

^aComparison shown for symmetrical cell method only

TABLE 5. PEARSON CORRELATION COEFFICIENT OF α WITH OTHER HALO PARAMETERS

	M_v	λ	c	S_j	α_{cell}^{sym}	α_{cell}^{norm}	α_{DM}^{par}
α_{GAS}^{par}	-0.12	0.27	-0.14	-0.04	0.51	0.86	0.69
α_{DM}^{par}	-0.16	0.53	-0.25	0.27	0.76	0.80	1.00

NOTE. — The superscript on α denotes the method employed to calculate the AMD e.g particle method , symmetrical cell method or normal cell method (free from symmetry restriction).

6.3. Comparison of quality of α and μ fits

It might sound strange that two different functional forms are being used to describe the same data. But it is not very surprising considering the fact that the profiles cannot be perfectly described by a functional form, they have small deviations and this gives enough room to both μ or α profiles (which after all are not very different) to be used to fit them with equally good fits. The profiles from the cell method (symmetrical) tend to have an abrupt truncation at $j = j_{max}$ for some cases (probably due to the symmetry effects discussed in previous section and also because the number of data points used to sample the profile, which is the total number of cells is small, typically around 60). So μ profiles which by design have an abrupt truncation at $j = j_{max}$ perform better in the outer regions for these cases, but for the same reason they are not able to fit the particle profiles in the outer regions which have a smooth extended tail. The α profiles fare better for these. So if we neglect the outer parts $P(< s) > 0.95$ then both the profiles provide a satisfactory fit to the distributions from both methods. To get an estimate of the quality of the fits, we measure χ^2 for data points with $P(< s) \leq 0.95$ for both profiles. χ^2 is defined as $\chi^2 = \sum_{i=1}^N ((y_i^{data} - y_i^{model})/\sigma_i)^2$ for each of the fits. To make a comparison we calculate the median of $(\chi_\alpha^2 - \chi_\mu^2)/(\chi_\alpha \chi_\mu)$ and median of χ_α^2/χ_μ^2 over all the halos. If the χ^2 for both of them are equal then the former quantity is close to zero. A negative value of -1 implies $\chi_\mu^2 = 2.5 \chi_\alpha^2$. If the median of χ_α^2/χ_μ^2 is close to 1 then both fits are good for equal percentage of halos. If more than 50% of halos have $\chi_\alpha < \chi_\mu$ then the above quantity will be less than 1 and vice versa. In Table 4 and Table 5 the values of these quantities are listed for various methods. Form the table we can see that both the profiles are equally good at describing the AMDs obtained by symmetrical cell and particle methods (except for the outer 5%).

7. CONCLUSION & DISCUSSIONS

We have presented here results from the non-radiative hydrodynamical simulation of 41 high resolution halos whose masses were selected to span the range from dwarf to bright galaxies. Our investigation mainly focused on the angular mo-

mentum properties of the halos and whether there are systematic differences between gas and dark matter. Our findings can be summarized as follows:

1. We investigated some of the global angular momentum properties like spin parameter λ , fraction of negative angular momentum f and misalignment angle θ . We find the spin parameter of gas to be on average larger than that of DM and this effect is systematically more pronounced at lower redshifts. At $z=0$ $\lambda_{gas}/\lambda_{DM} \sim 1.4$, which is in agreement with the result reported by CJ02, but is not in agreement with vB2002 who do not find any such bias. The mean of the misalignment angle θ is 20° which is again in agreement with CJ02 who get a value 23.5° but is less than the value of 36.2° obtained by vB2002. Both these discrepancies could be due to the inclusion of a large number of low resolution halos in the analysis of vB2002. The counter-rotating fraction f is anti-correlated with λ and for gas f decreases with decrease of redshift, an effect that can be explained by the increasing level of thermalization at lower redshifts. Other than this there is little evolution of other properties with redshift.
2. We find that the fraction of material with negative angular momentum can be described by the equation $f = 1 - I_g(\lambda/\lambda_0)$, with $I(x)$ being a Gaussian integral. To understand these effects we developed a toy model, where we introduce an ordered velocity v_o which is smeared by means of Gaussian random motion with dispersion σ . This model reproduces the $f = f(\lambda)$ correlation and suggests an actual relation of $f = 1 - I_g(1/\zeta)$ where $\zeta = \sigma/v_o$. This relation is demonstrated to be in excellent agreement with the results from simulations. We also see that the gas gets more and more thermalized at lower redshift resulting in σ/V_v to be smaller at lower redshifts, whereas λ and concentration c increases at lower redshifts. All these effects are contributing to the decrease of the amount of gas with negative angular momentum. The model also reproduces well the shape of AMD observed in simulations.
3. We study the distribution of angular momentum in detail, and compare and contrast various different techniques used to derive angular momentum distributions. We first use the cell method as proposed by B2001 and reproduce the result of CJ03 that μ for gas is greater than that of DM. We find that the results are sensitive to the very details of the method employed for fitting. In particular the effect of gas having higher μ is diminished to a large extent if fits are performed assuming a constant λ rather than a constant j_{max} . According to CJ03 μ for gas is comfortably in the range required by observation of disk galaxies which is ($\mu > 1.75$). We also find that about 30% of halos have $\mu > 1.75$.
4. By comparing the AMD found in the simulations with those of exponential disks we conclude that merely having $\mu > 1.75$ is not a sufficient condition to match the angular momentum profiles of observed disk galaxies. We find that a generalized profile, based on gamma distribution, with a single parameter α can be used to fit the AMD of model galaxies (exponential disks embedded in NFW halos) as well as AMD of gas and DM in simulations. $\alpha > 1.3$ seems to resemble the profiles of

dwarf galaxies shown in BBS01, a condition that is only obeyed by a small minority of halos (less than 10%). For fits based on the (symmetric) cell method only 10% of the halos have gas with $\alpha > 1.3$ (after rejecting halos with bad fits). For particle method and normal cell method the percentage is even lower, about 2% of halos have $\alpha > 1.3$. We find the particle method to be more robust, with data that is less noisy and also free from any artificial non local averaging or any symmetry assumptions. The profile in particle method do not have abrupt truncation like in cell method (symmetrical) and are more extended. This may have important implications for the truncation radius and extent of gas in real disks: In semi analytical models the distribution and extent of cold gas depends upon the AMD used for the models. In van den Bosch (2001)(Fig-9 there) the models have an AMD with μ between 1.6 and 1.9, and the disks are predicted to have a sharp truncation ($R_{\text{gas}}/R_{\text{HI}} \sim 1$) of cold gas which is in disagreement with observed distribution of HI in galaxies ($R_{\text{gas}}/R_{\text{HI}} > 1.5$). Here R_{gas} is the maximum extent of gas with non zero surface density and R_{HI} is the radius with surface density of $1 \text{ M}_{\odot} \text{ pc}^{-2}$.

5. For the particle method, there is a significant fraction of counter-rotating matter which has been excluded in calculating α . The final AMD (and therefore the predicted structure of the model galaxy) will depend strongly upon how this material eventually gets mixed up with the remaining portion of the halo, during the assembly of the galaxy. We saw that the counter-rotating matter undergoes extensive mixing during the history of its formation in the hierarchical framework. But the situation we have here is slightly different as it concerns the fate of the counter-rotating gas in an isolated halo when subjected to collapse. In the absence of any information it is best not to assume any preferential mixing with low, or high AM material or also equal AM material in which case it might form a non rotating bulge as prescribed in vB2002. The most plausible prescription seems to be that of random mixing: During collapse the counter-rotating matter will follow a slightly different

trajectory than normal matter around it and in the process it will get mixed by shocks with matter of various different AM along its path. This process does not seem to have any preference. If we assume that the process of mixing will not change the distribution of α significantly, we can conclude that less than 10% of halos have $\alpha > 1.3$. In other words only the absolute minority of halos have AM distributions that resembles that of an observed (dwarf or LSB) disk galaxy. In the absence of any significant correlation of α with mass M_v or for that matter with any other halo parameter, this leads us to the general conclusion that a typical halo in ΛCDM simulation has far too much low angular momentum material to account for majority galaxies featuring a dominated disk component.

6. If the angular momentum of each element is conserved then low angular momentum material has to be preferentially discarded during the process of galaxy formation, this might be effected by means of supernova feedback during star formation that drives out gas from small halos that come randomly from all direction and contribute mainly to the low angular momentum material as shown by Maller & Dekel (2002). The AMD of bright galaxies in Maller & Dekel (2002), which are effected little by feedback, seems to have $\alpha \sim 1$ (no dip in AMD for small s), consistent with AM profile of a galaxy with a bulge which accounts for the low AM material. It is no way similar to exponential disk with flat rotation curves as claimed there, because that would imply an $\alpha = 2$ and will be reflected as a prominent dip.

We are grateful to James Bullock and Daniel Eisenstein for stimulating discussions and also Vince Eke for his help with the initial conditions of the simulations. This work has been supported by grants from the U.S. National Aeronautics and Space Administration (NAG 5-10827), the David and Lucile Packard Foundation, and the Bundesministerium für Bildung und Forschung (FKZ 05EA2BA1/8).

REFERENCES

Barnes, J. & Efstathiou, G. 1987, ApJ, 319, 575
 Bryan, G. L. & Norman, M. L. 1998, ApJ, 495, 80
 Bullock, J. S., Dekel, A., Kolatt, T. S., Kravtsov, A. V., Klypin, A. A., Porciani, C., & Primack, J. R. 2001, ApJ, 555, 240
 Bullock, J. S., Kolatt, T. S., Sigad, Y., Somerville, R. S., Kravtsov, A. V., Klypin, A. A., Primack, J. R., & Dekel, A. 2001, MNRAS, 321, 559
 Chen, D. N. & Jing, Y. P. 2002, MNRAS, 336, 55
 Chen, D. N., Jing, Y. P., & Yoshikawa, K. 2003, ApJ, 597, 35
 Dalcanton, J. J., Spergel, D. N., & Summers, F. J. 1997, ApJ, 482, 659
 Efstathiou, G. & Jones, B. J. T. 1979, MNRAS, 186, 133
 Eke, V. R., Navarro, J. F., & Steinmetz, M. 2001, ApJ, 554, 114
 Fall, S. M. & Efstathiou, G. 1980, MNRAS, 193, 189
 Maller, A. H. & Dekel, A. 2002, MNRAS, 335, 487
 Melchiorri, A., Bode, P., Bahcall, N. A., & Silk, J. 2003, ApJ, 586, L1
 Mo, H. J., Mao, S., & White, S. D. M. 1998, MNRAS, 295, 319
 Navarro, J. F. & Benz, W. 1991, ApJ, 380, 320
 Navarro, J. F. & Steinmetz, M. 1997, ApJ, 478, 13
 Navarro, J. F. & White, S. D. M. 1994, MNRAS, 267, 401
 Navarro, J. F., Frenk, C. S., & White, S. D. M. 1996, ApJ, 462, 563
 Navarro, J. F., Frenk, C. S., & White, S. D. M. 1997, ApJ, 490, 493
 Peebles, P. J. E. 1969, ApJ, 155, 393
 Spergel, D. N. et al. 2003, ApJS, 148, 175
 Springel, V., Yoshida, N., & White, S. D. M. 2001, New Astronomy, 6, 79
 Steinmetz, M. & Bartelmann, M. 1995, MNRAS272, 570
 Steinmetz, M. & Navarro, J. F. 1999, ApJ, 513, 555
 van den Bosch, F. C., Abel, T., Croft, R. A. C., Hernquist, L., & White, S. D. M. 2002, ApJ, 576, 21
 van den Bosch, F. C. 2001, MNRAS, 327, 1334
 van den Bosch, F. C., Burkert, A., & Swaters, R. A. 2001, MNRAS, 326, 1205
 White, S. D. M. & Rees, M. J. 1978, MNRAS, 183, 341